Exploration of digital-filter and forward-stepwise synthetic turbulence generators and an improvement for their skewness-kurtosis

Kutalmis M. Bercin, Zheng-Tong Xie*, Stephen R. Turnock

Faculty of Engineering and the Environment, University of Southampton, SO17 1BJ, Southampton, the UK

Abstract

The performance of four synthetic turbulence generators that represent the majority of capabilities of *i*. digital-filter-based (DFM) and *ii*. forward-stepwise-based (FSM) generator categories is evaluated prior to transferring generator outputs into computational fluid dynamics simulations. In addition, a cheap-to-run and easy-to-code piecewise closed-form function that transforms one-spatial-point skewness-kurtosis of a synthetic time-series to a target value is derived and presented. The two main purposes of the study are to support model users in their decision process for choosing the most convenient type and their understanding of the models through a systematic exploration of model variables and modelling stages, and to extend the Gaussian nature of these models at a spatial point into non-Gaussianity for the first time. The evaluation test-bed contains three benchmarks, each of which focuses on an isolated aspect of turbulent flows: *i*. decaying homogeneous isotropic turbulence, *ii*. homogeneous shear turbulence and *iii*. plane channel flow with smooth walls. Results obtained reveal that: (i) the original DFM provides the highest level of reconstruction for input one-spatial-point second-order correlation tensors and two-spatial/temporal-point correlation functions; (ii) FSM yields the best trade-off between the computational cost and the level of reconstruction; (iii) the use of exponential-form correlation functions as a model approximation is more advisable than that of Gaussian-form, as the former removes the premature, sharp, flow-type-independent drop in power spectra observed for the latter; (iv) the proposed non-Gaussian functionality reconstructs the target one-spatial-point skewness-kurtosis pairs of the test-bed flows virtually without altering their already-embedded statistics; (v) the Lund transformation changes existing statistics only in statistically inhomogeneous lateral directions of a flow when anisotropic

* Corresponding author
Email address: Z.Xie@soton.ac.uk (Zheng-Tong Xie)

Reynolds stresses are present; and (vi) a spatial variation of correlation functions on turbulence generation plane improves the overall reconstruction fidelity in terms of correlation functions and power spectra.

Keywords: inflow turbulence, synthetic turbulence, inlet conditions, random flow generation, synthetic wind, non-Gaussian turbulence, non-Gaussian wind

1. Background to inflow turbulence generation

Turbulent flow regimes are the norm in nature; thus, significant to consider in engineering applications with reasonable fidelity. At many levels of industry and academia, the contemporary trend in turbulence modelling is away from semi-/empiricism towards first principles with minimal cost increase. This trend, however, poses substantial ongoing challenges, particularly for inflow boundary conditions of convective flows. In theoretical and numerical means, spatiotemporal delineation of these conditions, stochastically and statistically, is proved to be challenging mainly due to the chaotic dynamics of turbulence and various requirements on the fidelity.

For computational fluid dynamics (CFD), most of the inflow turbulence generation approaches aim to satisfy all or a part of the prescribed conditions, i.e. up to 2nd order statistics, integral length scales and Gaussian distribution of turbulent fluctuations. Some of them are also able to produce reasonable autocorrelation and spectrum. Only a very few synthetic turbulence generation approaches spend efforts on the 3rd order (skewness) and 4th order (kurtosis) statistics [1, 2]. Lack of high order statistics modelling for turbulence generation may significantly impact the modelling accuracy for some applications, such as wind loading [3, 4]. A rigorous assessment of the abilities of current synthetic turbulence generation approaches, and a simple and efficient model to generate non-Gaussian turbulence are of great interest.

Most of the inflow turbulence generation methods were classified into four main categories by [5]: *i*. library-based, *ii*. recycling-based, *iii*. transition inducement-based, and *iv*. synthetic methods.[1] The last category may further be divided into six subcategories on the basis of their methodology: *i*. linearised turbulence model-based [8], *ii*. Fourier-based [9, 10], *iii*. proper orthogonal decomposition-based [11], *iv*. synthetic-eddy-based [12], *v*. digital filter-based [13], and *vi*. forward stepwise-based [14]. In this study, the scope is limited to the last two subcategories (hereafter,

[1] [6, p. 553] and [7], however, regarded the first two as a single category.

DFM and FSM, respectively) whilst the two arguably demand the simplest code implementation, yet provide high model fidelity with relatively low computational costs. The reader is, therefore, referred to [6, 5, 7] for the other categories.

Fig. 1 shows that DFM or FSM transforms a given random number set to a spatiotemporally new set involving a group of *target* statistical measures.[2] A chain of arithmetic operations is performed for the transformation. Within the chain, the target statistics arrange the properties and order of the operations, so that the the *realized* statistics of the new sets could match the *target*.

Although Borgman [15] earlier elaborated on a method in which synthetic ocean wave processes are generated through digital filtering of a group of statistics and white-noise time-series[3], the contemporary DFM was introduced by [13], based on preliminaries from [16]. The authors developed a three-consecutive-stage framework: (*i.*) random number set generation, (*ii.*) embedment of arbitrary two-spatial-point autocorrelation functions through digital filters, and (*iii.*) incorporation of one-spatial-point second-order correlation tensor by a tensor transformation [17] (hereafter, the Lund transformation). In addition, the authors simplified the second-stage by restricting autocorrelation functions to Gaussian-form, so that filter coefficients can be explicitly evaluated, whose evaluation requires a root-finding algorithm otherwise. The function-form choice was justified with the same form observed in the viscous-dissipation stage of homogeneous isotropic turbulence.

In this initial DFM, five principal limitations exist, which subsequent studies attempted to alleviate: output (*i.*) contains no physical information beyond input statistics, (*ii.*) can only be generated on Cartesian grids[4], (*iii.*) is not divergence-free, (*iv.*) is statistically stationary, and (*v.*) obeys Gaussian probability density function (PDF) at a spatial point.

For the first limitation, di Mare et al. [18] investigated the possibility and practical viability of inserting arbitrary-form autocorrelation functions into the second model-stage. They proposed a new algorithm in which standard linear algebra tools are used to numerically solve a designed 'bilinear difference equation' to obtain digital-filter coefficients corresponding to the given autocorrelation function. The authors held the view that [13, p. 658]'s simplification is decent for free-shear flows whereas their more-information-carrying algorithm appears advisable for wall-bounded flows [18,

[2] Measures predominantly consist of *i.* one-spatial-point second-order correlation tensor (i.e. Reynolds stress tensor) and *ii.* two-spatial/temporal-point autocorrelation functions.

[3] *White-noise* refers to a uniform power distribution across a frequency spectrum. By contrast, herein, the *Gaussianity* of a time-series will only refer to the probability distribution of amplitude

[4] A *Cartesian* grid herein refers to a grid wherein cells are unit squares/cubes.

p. 10]. Afterwards, di Mare and Jones [19, p. 687] put forward another algorithm, which was presented as computationally cheaper, more competent and robust in comparison to their previous algorithm. Further, Fathali et al. [20, p. 96] claimed that the third model-stage distorts the resultant statistics from the second model-stage for highly anisotropic flow fields. On this basis, the authors put forth a two-stage-unified framework, which aimed to remove distortions and embed two-spatial-point cross-correlations. Subsequently, Xie and Castro [14] argued that the exponential-form functions are more appropriate simplification than [13]'s Gaussian-form, specifically for turbulent shear flows. Furthermore, the authors derived FSM which was quantified equivalent-in-effect to, and yet cheaper-to-compute than more complex digital filters. Then, the second model-stage of DFM in the streamwise direction was substituted with FSM; thus, resulting in a hybrid DFM-FSM.

The second limitation was, on the other hand, not shared by FSM, with which synthetic time-series generation on non-uniform grids is possible. For DFM, however, Kempf et al. [21] replaced the second model-stage with a diffusion process deemed equivalent to digital filtering, so that synthetic time-series can be seamlessly generated on non-uniformly spaced grids or on arbitrary boundary geometries. In addition, Fru et al. [22, p. 328] purported that a hybrid of the methods from [13] and [21] was developed, which is allegedly immune to this limitation. The authors, however, failed to clearly describe what the new method is. Lastly, Dhamankar et al. [23] enabled DFM to be used in curvilinear structured grids without interpolations through generating time-series on a Cartesian grid which is inherently a one-to-one-mapped corresponding curvilinear grid. Although the approach worked round interpolation errors, new drawbacks of their own arose [23, p. 11].

The third limitation reportedly causes erroneous pressure fluctuations [24, p. 1089], which was quantified by [25, Fig. 11] for incompressible plane channel flows wherein several orders of magnitude over-predicted pressure fluctuations persistent across the computational domain were observed. In contrast, negligible alterations due to non-divergence were expected and reported for velocity fluctuations [21, p. 76], [25, Fig. 11]. In general, therefore, it seems that non-divergence can be anticipated influential solely on computations where pressure is the principal field of interest. Considering these implications, divergence-freeness was first imposed into DFM for homogeneous isotropic turbulence by [26, p. 5] through devising solenoidal digital filters. For non-homogeneous anisotropic turbulence, on the other hand, [26, p. 7] was contented with a suggestion to use [27, p. 3-5]'s transformation method. Similarly, Kelein et al. [13, p. 659] and Kempf et al. [21, p. 76] suggested a projection method from [10] in order to divergence-free transition synthetic time-series.

None of the two suggestions were, however, tested to date. From another viewpoint, Kim et al. [25] rendered the hybrid DFM-FSM divergence-free by directly embedding synthetic time-series into the momentum predictor equation in a pressure-velocity coupling algorithm, in which case any non-solenoidal velocity field could be transformed without additional costs.

Regarding the fifth limitation, which was not studied in the DFM/FSM literature to date, evidence suggests that the frequency of occurrence of various turbulence characteristics tends to follow non-Gaussian distributions at a single spatial point. For instance, Jimenez [28] reviewed the literature that the one-spatial-point Pearsonian coefficient of kurtosis is approximately 2.85 (rather than 3.00) for velocity fluctuations in homogeneous isotropic turbulence. Even more pronouncedly, Moser et al. [29] reported for Re=395 plane channel flow that the one-spatial-point Pearsonian coefficient of skewness and kurtosis of velocity fluctuations vary across from -0.8 to 0.4, and from 2.1 to 38.0, respectively.[5]

Apart from the above, eight more studies offered major changes in various topics. For instance, Touber and Sandham [30, p. 104-105] systematically extended the hybrid DFM-FSM to compressible flows by generating thermodynamic fluctuations with synthetic velocity fluctuations via 'the strong Reynolds analogy'. Furthermore, Breuer and Schmidt [31, p. 677] expanded DFM to be utilised on interfaces of a hybrid LES-URANS methodology by formulating a modelled kinetic energy equation as a function of synthetic velocity fluctuations. Moreover, Anupindi and Sandberg [32, p. 703] seamlessly coupled, stricter than the aforementioned, the hybrid DFM-FSM into another LES-RANS methodology, wherein flow quantities at RANS-side of an interface are time-accurately sampled to create synthetic time-series at LES-side. Additionally, Okaze and Mochida [33, p. 25] modified the Lund transformation of the hybrid DFM-FSM to include scalar fluctuations and their complete correlations with flow variables although previously [34, p. 1313] utilised DFM to prescribe spatiotemporally-variant scalars by omitting their flow-cross-correlations. The hybrid DFM-FSM of [14] was extended by [35] with replacing DFM in all directions; hence, leading to 'pure' FSM. Last but not least, Schmidt and Breuer [36] designated an approach where synthetic time-series are introduced into a computational domain via source terms in the momentum equation in order to freely determine the boundary location.

[5] *Skewness* and *kurtosis* quantify the extent of PDF asymmetry and tail shape deviating from the normal distribution, respectively. Qualitatively, the former shows the dominant sign of the deviations from the mean turbulence quantities, and the latter the frequency of occurrence of extreme events in turbulence.

In DFM/FSM theory, arguably, no fundamental development was followed. Nevertheless, transferable performance improvements were put forth for the two DFM/FSM steps which are the costliest: (*i.*) digital filtering, and (*ii.*) generation of Gaussian random number sets. For the former, Veloudis et al. [37, p. 9] advanced filtering in frequency domain, which may reduce floating-point operations per time-step (FLOPT) from $\mathcal{O}(n^i)_{\{n\in\mathbb{N};\, i\in\{1,2,3\}\}}$ to $\mathcal{O}(n\log_i n)$. Additionally, Veloudis et al. [37, p. 10] assessed the potentiality of time-step reductions of synthetic time-series generation within a more restrictive environment (e.g. LES) without deteriorating temporal accuracy. Alternatively, Kempf et al. [38] propounded filtering via the 'separable convolution summation method' [39, p. 404] where convolution summations are consecutively performed on number sets along each coordinate. As a result, a speed-up of FLOPT from $\mathcal{O}(n^i)_{\{i=3\}}$ to $i\mathcal{O}(n)_{\{i=3\}}$ may be observed. Furthermore, the authors devised a parallelization procedure with zero-inter-communication by seeding pseudo-random number generators with constant pairs of integers and corresponding grid node indices. For the latter cost source, Xie and Castro [14] manipulated $\mathcal{O}(10)$ uniformly-distributed random number sets into normal samples through the central limit theorem. By contrast, Touber and Sandham [30, p. 104-105] asserted that the Box-Muller's theorem can reduce the number of these sets to two.

Besides the known limitations, previous studies failed to fill knowledge gaps in three main areas. First, although a number of independent and consecutive model stages form DFM/FSM, no investigation was made on to which extent each stage performs its task in isolation and interacts with the others. Second, all the research to date quantified DFM/FSM as a whole with CFD whereas the both are separate entities, and the latter causes metamorphosis of time-series produced by the former. Therefore, the performance of DFM/FSM *itself*, without the impact of CFD, remains unquantified. Third, most existing accounts either did not consider 'building-block' flows to evaluate DFM/FSM (e.g. no homogeneous isotropic/shear turbulence study was performed with [14].) or did not contain the complete set of *fundamental* assessment measures (e.g. [13] did not provide any results of power spectral density function.).

The lack of structured knowledge in the three areas, however, hinders any attempts for theoretical capability-oriented improvements in DFM/FSM, for conveying their benefits to a wider audience, as well as for decision-making of the most appropriate variant to the problem at hand. The aims of this study are therefore *i.* to advance our understanding of the aforementioned knowledge gaps with the help of systematic explorations of model parameters and stages, and *ii.* to

improve DFM/FSM capability portfolio through implementing a non-parametric one-spatial-point skewness-kurtosis transformation functionality.

To this end, a brief description of four synthetic turbulence generators including DFM and FSM is presented in §2, and the new one-spatial-point non-Gaussian functionality is described in §3. §4 presents three benchmark flows for tests and the statistical measures used. The obtained results including the assessment of the four synthetic turbulence generators and the new functionality are illustrated in §5. Clear-cut conclusions alongside a discussion on remaining challenges are listed in §6.

2. A brief description of four synthetic turbulence generators

2.1. Digital-filter-based and forward-stepwise-based synthetic turbulence generators

DFM and FSM construct spatiotemporal-variant Reynolds-decomposed fluctuation velocity (or scalar) fields, $\{u_i'(\mathbf{x},t)\in\mathbb{Q}\}_{\{i\,\in\,\mathbb{N}\,:\,i\,\in\,[1,3];\,t>0\}}$. Both generators may be abstracted into four consecutive and independent model stages as shown in Fig. 2 for a one-dimensional field of discrete points.

The first stage is the generation of a set of random numbers, $\{\mathrm{r}\}_{\{|\mathrm{r}|=\mathrm{R};\ \mathrm{k,j}\,\in\,\mathbb{N}\,:\,1\leq\mathrm{k+j}\leq\mathrm{R}\}}$, obeying the PDF of zero-mean ($\mathrm{R}^{-1}\sum_{\mathrm{k}=1}^{\mathrm{R}}\mathrm{r_k}=0$), unit-variance ($\mathrm{R}^{-1}\sum_{\mathrm{k}=1}^{\mathrm{R}}\mathrm{r_k^2}=1$), independent ($\mathrm{R}^{-1}\sum_{\mathrm{k}=1}^{\mathrm{R}}\mathrm{r_k r_j}=0$ for $\mathrm{k}\neq\mathrm{j}$) Gaussian white-noise.

In the second stage, a set of numbers 'calibrated' to two-spatial/temporal-point correlation functions, {b}, is generated. With DFM, the set is computed by Klein et al.'s [13, p. 657] relation between {b} and an autocorrelation function, ρ:

$$\rho\left(\mathrm{q,p}\right)=\underbrace{\frac{\overline{u_\mathrm{p}'u_{\mathrm{p+q}}'}}{\overline{u_\mathrm{p}'u_\mathrm{p}'}}}_{\text{known}}=\underbrace{\frac{\sum_{\mathrm{j}=-\mathrm{N}+\mathrm{q}}^{\mathrm{N}}\mathrm{b_j b_{j-q}}}{\sum_{\mathrm{j}=-\mathrm{N}}^{\mathrm{N}}\mathrm{b_j^2}}}_{\text{unknown}}\tag{1}$$

where $\mathrm{q}_{\{\mathrm{q}\in\mathbb{N}\,:\,\mathrm{q}\geq0\}}$ is the lag number, p the maximum lag number, $\{\mathrm{b}\}_{\{|\mathrm{b}|=2\mathrm{N}+1\,:\,\mathrm{b}\in\mathbb{Q}\}}$ a set of filter coefficients, and $\{\mathrm{N}\}_{\{|\mathrm{N}|\in\mathbb{N}\,:\,\mathrm{N}>0\}}$ the support of a filter. The diversity in DFM mainly arises from the different expressions proposed to invert Eq. 1. In contrast, in FSM, {b} is redefined by a group of integral length-scales weighted with empirical constants and limits of integration.

In the third stage, {b} is embed into {r} via a mathematical operation, so that a new set, $\{s\}$, is constructed with a new spatiotemporal stochastic pattern and yet consisting of correlation function statistics. While FSM simply uses element-wise multiplication, DFM utilises convolution summation as follows:

$$s_{\mathrm{k}} \equiv \mathrm{F_N}\left(\mathrm{k}\right) = \sum_{\mathrm{j}=-\mathrm{N}}^{\mathrm{N}} \mathrm{b_j r_{k+j}} \tag{2}$$

where $\{s\}_{\{|s|=\mathrm{M}\,:\,s\in\mathbb{Q}\}}$ is a set of digital-filtered numbers, and $\mathrm{F_N}$ a linear, non-recursive, discrete filter operator performing a convolution summation on two finite sequences. In $\mathrm{F_N}$, the two sets must completely overlap; thus, producing only a subset of the conventional *full* convolution summation. Accordingly, the size of the sets is related as: R-(2N+1)+1=M.

In the last stage, the one-spatial-point correlation tensor is incorporated into $\{s\}$ through the Lund transformation [17, p. 255]: $u_i'\left(\mathbf{x},t\right) = a_{ij}(\mathbf{x})\; s^i(\mathbf{x},t)$ where a_{ij}, a spatial-variant amplitude tensor of second-order, is shown below:

$$a_{ij} = \begin{bmatrix} (R_{11})^{0.5} & 0 & 0 \\ R_{21}/a_{11} & (R_{22}-a_{21}^2)^{0.5} & 0 \\ R_{31}/a_{11} & (R_{32}-a_{21}a_{31})/a_{22} & (R_{33}-a_{31}^2-a_{32}^2)^{0.5} \end{bmatrix} \tag{3}$$

where R_{ij} is the (known) one-spatial-point correlation tensor in units of variance. It should be noted that a_{ij} is conventionally spatial-variant and temporal-invariant whereas there is no theoretical objection to its temporal variation.

2.1.1. Klein et al.'s method - DFM

Klein et al. [13, p. 657-658] approximated the right-hand side of Eq. 1 as a Gaussian-form function of integral length-scales, so that {b} can be explicitly evaluated. The proposition was justified with the fact that autocorrelation functions of late-stage homogeneous turbulence have Gaussian-form. For a computational grid of cubic cells with $\{\Delta_i\}_{\{i\in[1,3]\}}$, constant grid size in a specific direction, the approximation to Eq. 1 in its discrete-form is shown below:

$$\rho \approx \exp\left(-\frac{\pi}{4}\,\frac{(m_i\,\Delta_i)^2}{(n_i\,\Delta_i)^2}\right) = \exp\left(-\frac{\pi}{4}\,\frac{m_i^2}{n_i^2}\right) \tag{4}$$

where m is the rectilinear distance of the node in question to the zero-lag correlation node, and n the length-scale size. Both are in grid spacing units. Correspondingly, Klein et al. [13, p.658] derived a closed-form expression for $\{\mathrm{b}\}$:

$$\{\mathrm{b}\}_i \approx \widetilde{\{\mathrm{b}\}}_i \Big/ \left(\sum_{\mathrm{j}=-\mathrm{N}}^{\mathrm{N}} \widetilde{\mathrm{b}}_{\mathrm{j}}^2 \right)^{0.5} \quad \text{as} \quad \widetilde{\{\mathrm{b}\}}_i = \exp\left(-\frac{\pi}{2} \frac{m_i^2}{n_i^2} \right) \tag{5}$$

The validity of the approximation was shown to have two constraints: *i*. the length-scale size is limited to the range $2 \leq n_i \leq 100$, and *ii*. the support of the filter must at least be two times the scale size, $\mathrm{N}_i \geq 2n_i$.

2.1.2. A customized method in spirit of di Mare et al.'s method - DFM

The possibility of the direct inversion of Eq. 1 was investigated by [18] through an iterative root-finder algorithm of Newton's method, so that arbitrary-form of correlation functions could be used in DFM. The main disadvantage of this method is arguably deemed to be its difficult code implementation. In this study, for this reason, a new approach with the *spirit* of [18] was invented as follows. First, a given arbitrary-form correlation dataset is curve fit to a chosen-form of a continuous function. Then, the direct inversion of Eq. 1 is conducted on this curve-fit function. Accordingly, for the study's set of benchmarks, the following expression was devised as the most proper form of the function:

$$\{\mathrm{b}\} = \mathscr{R}\left[\rho\right] = \mathscr{R}\left[\mathscr{C}\left\{a \exp(-b\,x) + c \exp(-d\,x)\right\}\right] \tag{6}$$

where $\mathscr{R}$ denotes the chosen root-finder algorithm, $\mathscr{C}$ the curve-fit algorithm, and $\{a, b, c, d\}_{\{\forall \in \mathbb{Q}\}}$ are the curve-fit parameters. Herein, filter supports are sized to the point where correlation functions drop below few percent of their zero-lag value.

2.1.3. Xie and Castro's method - Hybrid DFM-FSM

In contrast to [13], Xie and Castro [14, p. 454] modelled the right-hand side of Eq. 1 as an exponential-form function, which was deemed more valid for turbulent shear flows:

$$\rho \approx \exp\left(-c\,\frac{\pi}{2}\,\frac{|m_i|}{n_i} \right) \quad \text{resulting in} \quad \widetilde{\{\mathrm{b}\}}_i \approx \exp\left(-c\,\pi \frac{|m_i|}{n_i} \right) \tag{7}$$

where c=1 is a constant. Furthermore, to reduce computational costs, the streamwise convolution summation in DFM was replaced by a simpler and a quantitatively justified equivalent procedure, named FSM [14, p. 456]. Therein, streamwise integral length-scales are input through temporal-correlation of two planes of $\{s^i\}$, which are generated at successive time-steps:

$$s^{i\Psi}\left(y,z,t{+}\Delta_t\right) = s^{i\Psi}\left(y,z,t\right)\exp\left(\text{-}c\,\frac{\pi}{2}\,\frac{\Delta_t}{\mathrm{T}}\right) + s^{i\psi}(y,z,t{+}\Delta_t)\left\{1\text{-}\exp\left(\text{-}c\,\pi\,\frac{\Delta_t}{\mathrm{T}}\right)\right\}^{0.5} \tag{8}$$

where $\{s^{i\Psi}\}$ is a temporal slice of $\{s^i\}$ including transverse length-scales $\{\mathrm{L}_\alpha\}_{\{\alpha\in\{y,z\}\}}$ at time t, $\{s^{i\psi}\}$ an auxiliary temporal slice generated with a new set of random numbers in the same way with $\{s^{i\Psi}\}$, T streamwise Lagrangian time-scale computed with Taylor's frozen turbulence hypothesis [40].[6]

In their discussion of the default value of c=1, Kim et al. [25, p. 57] put forth c=0.5 is more apt to use for their plane channel flow CFD simulations. In view of this statement, herein, three values of c=$\{1, 0.5, 0.25\}$ were tested via the three benchmark flows without CFD (§4.1). For the majority of the scenarios, c=0.5 yielded the highest level of similarity to the benchmarks in terms of correlation functions and power spectra (not reported). Therefore, Kim et al. [25]'s preference was used throughout the study as the default model constant instead of the original value of c. It should be stressed that c=0.5 is not universal, yet a solution of model calibration to the flows in question. One may thereby seek other values of c for other types of flows.

2.1.4. Kim et al.'s method - FSM

Xie and Castro's [14] one-direction of FSM was extended to all directions by [35, p. 135]; hence, leading to abolishing the use of convolution summations of DFM. FSM is subsequently applied to

[6] According to the hypothesis: L_x=U_x T, where L_x is a streamwise integral length-scale, U_x, mean flow speed in the same direction, and T streamwise Lagrangian time-scale.

each direction in an arbitrary order to yield $\{s^i\}$ as follows:

$$s_y^i\,(t, j{+}1, k) = s_y^i\,(t, j, k) \exp\left(-\frac{c_y}{n_y}\right) + \mathrm{r}\,(t, j, k)\left\{1 - \exp\left(-\frac{2c_y}{n_y}\right)\right\}^{0.5} \tag{9a}$$

$$s_{yz}^i\,(t, j, k{+}1) = s_{yz}^i\,(t, j, k) \exp\left(-\frac{c_z}{n_z}\right) + s_y^i\,(t, j, k)\left\{1 - \exp\left(-\frac{2c_z}{n_z}\right)\right\}^{0.5} \tag{9b}$$

$$s_{yzx}^i\,(t{+}1, j, k) = s_{yzx}^i\,(t, j, k) \exp\left(-\frac{c_x}{n_x}\right) + s_{yz}^i\,(t, j, k)\left\{1 - \exp\left(-\frac{2c_x}{n_x}\right)\right\}^{0.5} \tag{9c}$$

where $\{c_i(\mathbf{x})\}_{\{i\in\{x,y,z\}\}}$ is a set of constants to scale $\{n_i\}$, and $\{\mathrm{r}\}$ *a* planar set of random numbers.

3. Development of the one-spatial-point non-Gaussian functionality

Transformation of skewness-kurtosis pairs of DFM/FSM at a spatial point was studied by means of three new approaches: *i*. non-Gaussian random number set input-based approach, *ii*. deterministic deconvolution-based approach, and *iii*. PDF transformation-based approach. The tests showed that the first two proposed approaches were proved to be ineffective, and the third approach to be promising, which is accordingly introduced in the following. It is however still deemed to present what the first two *sound* methods are for the reader's examination; thus, presented in §A.1-2.

3.1. PDF transformation-based approach

The approach is based on a transformation function. It is introduced as a new model stage between the 3rd and 4th stages illustrated in Fig. 2. The function is a piecewise closed-form function shown in Eq. 11, which was derived by means of two concepts: *i*. the memoryless nonlinear transformation method (MNT; also known as the *zero-memory non-linear transformation*) [41, 42], and *ii*. the Johnson system of PDFs [43].

MNT is the core concept of the current family of non-Gaussian process generation methodologies. Its main formulation was proposed by [42, p. 611] as:

$$\text{ю}_i'(\mathbf{x}, t) = g_i\{u_i'(\mathbf{x}, t)\} = F_{\text{ю}_i'}^{-1}\left\{\phi_{u_i'}\{u_i'(\mathbf{x}, t)\}\right\} \tag{10}$$

where u_i' is a process (known input) obeying a source PDF, $\text{ю}_i'$ corresponding transformed process (unknown output) obeying a target PDF, $\phi_{u_i'}$ the source cumulative distribution function (CDF), and $F_{\text{ю}_i'}^{-1}$ the target inverse CDF. The condition of the existence of the relation is satisfied if

$g_i\{\cdot\}$=$F^{-1}_{\text{ю}'_i}\{\phi_{u_i}\{\cdot\}\}$ is a monotonic function. Through the concept, a given u'_i, obeying a Gaussian CDF $\phi_{u'_i}$, could be transformed into a new process, $\text{ю}'_i$, obeying a target non-Gaussian CDF $F_{\text{ю}'_i}$.

The first potential drawback associated with the use of sole MNT is that Eq. 10 may modify spectral contents of u'_i towards $\text{ю}'_i$ [44, p. 19] due to the non-linearity of the function [45, p. 1196]. Whereas, as a rare counter-argument,Smallwood [46, p. 3] claimed that no substantial change should be expected in the spectral content of u'_i, because this is mostly determined by zero-crossings, which are not significantly altered by Eq. 10. The second drawback is the high computational cost of interpolations to execute Eq. 10 for each spatial-temporal point of random processes obeying arbitrary-form PDFs.

For a process, arbitrary-form non-Gaussianity implies infinite combinations of infinite-order non-standard moments; hence, has a broad meaning. In the context of turbulence, however, non-Gaussianity may be restricted to non-standard skewness and kurtosis only due to the fading physical interpretation of the ever-increasing level of abstraction in higher moments and their diminishing distinguishable impact on the physicality of turbulent flow developments.

With this constraint, identification of a unique and closely-approximated non-Gaussian distribution that can be customized to any valid combination of the first four central moments may be achieved through the Johnson system of distributions [43]. This system includes all valid skewness-kurtosis pairs (illustrated in [47, Fig. 1]) through its three members: *i*. S_U unbounded, *ii*. S_L log-normal (a transition line from *i* to *iii*) and *iii*. S_B bounded families [43, p. 156]. The readers are referred to [47] for the basic characteristics of the system.

More importantly, the substitution of the Johnson system into Eq. 10 yields a piecewise closed-form expression for $\text{ю}'_i$, which is easy-to-code and cheap-to-execute, as follows (for derivation details, refer to §A.3.1):

$$\text{ю}'_i(\mathbf{x},t)=\begin{cases}\dfrac{1}{\sigma_U}\left\{\sinh\left(\dfrac{u'_i(\mathbf{x},t)-\gamma}{\delta}\right)\text{-}\mu_U\right\}, & \text{for } S_U \text{ - Unbounded}\\ \exp\left\{u'_i(\mathbf{x},t)\right\}, & \text{for } S_L \text{ - Log-Normal}\\ \dfrac{1}{\sigma_B}\left[\left\{1+\exp\left(\dfrac{\gamma-u'_i(\mathbf{x},t)}{\delta}\right)\right\}^{\text{-}1}\text{-}\mu_B\right], & \text{for } S_B \text{ - Bounded}\end{cases} \tag{11}$$

where $\gamma(\beta_1,\beta_2)$ and $\delta(\beta_1,\beta_2)_{\{\delta>0\}}$ are the shape parameters of the Johnson system, $\mu_{U/B}(\gamma,\delta)$-

$\sigma_{U/B}(\gamma, \delta)$ the first two *theoretical* normalized moments of the corresponding families, $\beta_1^{0.5}$=μ_3/σ^3 and β_2=μ_4/σ^4 the Pearson's moment coefficient of skewness and kurtosis, μ_3 and μ_4 the third and fourth central moments, and σ the standard deviation. The expression leads to two further questions: for a (β_1, β_2)-pair, *i*. how to choose the appropriate family, and *ii*. how to compute γ-δ.

The criteria to choose one of the families rely on the relative position of the target skewness-kurtosis pair values with respect to the Cullen and Frey graph's log-normal curve [47, Fig. 1]. The curve was obtained by a parametric system of equations in [43, Eq. 14]. The set of equations, however, does not lend itself to a direct relation between skewness and kurtosis; thus, resulting in difficulties in the selection. Such functional relation, $g(\beta_2) \sim \beta_1$, was then derived by [48], and summarized in Eq.s (A.46) to (A.50). Accordingly, the following conditionals determine the family member: S_U, if $g(\beta_2)$>β_1; S_L, if $g(\beta_2)$=β_1 and S_B, if $g(\beta_2)$<β_1. In addition, the region wherein pairs cannot exist was defined as: β_2-β_1-1<0 [43, Fig. 2].

After finding the family that the pair belongs to, γ-δ can be computed through a *moment-matching technique*, where the family's theoretical expressions of skewness-kurtosis are solved for γ-δ with the help of root-finding algorithms. Parameterizations which considerably reduced the complexity of the root-finding problem were proposed by [48, p. 310] for S_U, and [49, p. 746-748] for S_B. Herein, these set of equations were manipulated in compliance with the requirements of the study and reported in Eq.s (A.12) to (A.17) for S_U and Eq.s (A.18) to (A.45) for S_B.

Table 2 compares the typical number of computational operations performed by Eq. 10 and 11. As shown, the new method eliminated all algorithms and reduced the number of elementary function operations. Moreover, the data preprocessing demand is less for the new method. For instance, the pairing between γ-δ and β_1-β_2 is a bijection; therefore, for each β_1-β_2 pair, γ-δ is computed only *once and for all* whereas, for the same β_1-β_2 pair, Eq. 10 needs to store an interpolation table of $F_{\text{IO}_i'}^{-1}$ values that also need to be computed by numerical integrations. Spatial-variation of β_1-β_2 across inflow plane, on the other hand, exponentially amplifies this contrast.

4. Methodology

4.1. Benchmarks and numerical settings

The four methods and the non-Gaussian approach were implemented into OpenFOAMv1612+ [50], and tested through a test-bed of three benchmark flows. The methods sorted by descending theoretical FLOPT are labelled as: *i*. Custom [18], *ii*. Klein et al. [13], *iii*. Xie-Castro [14], and *iv*. Kim

et al. [35]. The chosen methods represent the majority of DFM/FSM capabilities and varieties. The test-bed involves three 'building-block' flows: *i*. decaying homogeneous isotropic turbulence (HIT; the case of M=0.0508) [51], *ii*. homogeneous shear turbulence (HST; the case of h=0.305) [52], and *iii*. plane channel flow with smooth walls (PCF; the case of Re_τ=395) [29], each of which focuses on an isolated aspect of turbulent flows. In this study, the finite-volume method and Navier-Stokes equation models were turned off in order to prevent any hard-to-measure distortions in output statistics of the methods. The details of the benchmarks and numerical set-ups are given in the following.

4.1.1. Common numerical settings

Each benchmark reports measurements for several test sections. For each benchmark, one of these sections was chosen, and corresponding time-variant planar flow field was approximately reconstructed by the methods. Then, the level of reconstruction was evaluated through a set of statistical measures shown in Table 1.

The dimensions of the planar physical sections were replicated in the numerical models. A Cartesian coordinate system in an inertial frame of reference, $\mathscr{I}$=$(\mathcal{O}, \mathbf{e}_x, \mathbf{e}_y, \mathbf{e}_z)$, was defined by $(x, y, z)_{\mathscr{I}} \equiv (1, 2, 3)_{\mathscr{I}}$ wherein x is the longitudinal (mean flow direction), y the vertical, z the transversal axis (statistically homogeneous direction for HST and PCF), and $\mathcal{O}$ the origin at the left-bottom corner of the planar numerical domain.

Three grids with the refinement ratio of 2.0 were generated for each benchmark. The planar domains were uniformly discretized into squares whose centroids store synthetic turbulence fields. Estimations for the upper- and lower-limits of the spatial resolutions were made in accordance with large eddy simulation (LES) requirements. An upper limit may be deemed as the minimum spatial resolution required for a conservative direct numerical simulation: $\Delta \lessapprox 2(\nu^3 \mathrm{L}\mathrm{U}_\mathrm{c}^{\text{-}3})^{0.25}$ where Δ is the isotropic grid spacing, ν the kinematic viscosity of flow, L isotropic integral length-scale, and $\mathrm{U_c}$ the characteristic flow speed.[7] A lower limit, as proposed by [54, p. 62], may be set $\Delta \approx 0.1\mathrm{L}_\epsilon$, where L_ϵ is an integral dissipation scale, and order of L [54, p. 53]. The spatial-compatible temporal resolution, Δ_t, was then computed considering the constraint of the theoretical pressure-velocity

[7] For the smallest resolved structure of size Δ, the maximum grid spacing could be 0.5Δ due to the Nyquist theorem [53, p. 10]. Assuming $\Delta \sim \eta$, where $\eta = (\nu^3/\epsilon)^{0.25}$ is the Kolmogorov length-scale and $\epsilon \sim \mathrm{U_c^3/L}$, then the maximum spacing roughly becomes $2(\nu^3 \mathrm{L}\mathrm{U}_\mathrm{c}^{\text{-}3})^{0.25}$.

coupling algorithm of PISO [55]: Δ_t<$U_c^{-1}\Delta$.

In order to make plausible inferences about the statistical population of interest, the minimum sample size required at a 98% confidence level, n_{min}, was estimated as 13000 elements via the following expression [56, §7.2.2.2.]: n_{min}=$(z_{1\text{-}\alpha/2}+z_{1\text{-}\beta})^2\sigma_{est}^2/\mathrm{CI}^2$ where z is the standard score in a normal distribution, α-β the type I-II error rates, σ_{est}=1 the forecasted standard deviation of the sample, and CI the confidence interval. Moreover, statistical convergence was qualitatively assessed through the time-series of the first four sample moments whereas no constraint, such an iterative linear solver requires, exists on the convergence.

4.1.2. Decaying homogeneous isotropic turbulence - HIT

HIT may be considered as the initial step in any turbulence model benchmarking whilst, in particular, any cross-correlation in its statistics is ideally zero. Through HIT, therefore, the isolated role of each model stage on the final output is expected to be revealed without cross interactions.

As a benchmark, from [51], the stationary-grid experiment of approximately isotropic decaying turbulent flow was used. The utilized experimental scenario belongs to the measurements at 42M downstream the turbulence generation grid, where M=0.0508[m] is the grid mesh size. At 42M, the mean longitudinal flow speed is U_c=12.7[ms^{-1}], and Reynolds number based upon Taylor micro-scale, λ, is Re_λ=71.6. For the non-Gaussianities in HIT, Jimenez et al. [57, p. 71] numerically and [28, p. 146] theoretically demonstrated that $\widehat{\beta}_2 \approx 2.85$, which is independent of Re [57, p. 70].[8] The set of input statistics is comprised of one-spatial-point normal-anisotropic correlations, and longitudinal and transverse integral length-scales, which respectively are: $\{\overline{(u'_{ii})^2}\}_{\{i\in(1,2,3)\}}$=0.049284[m^{2}s^{-2}], $\{\overline{(u'_{ij})^2}\}_{\{i\neq j\}}$=0.00, L_{long}=0.024[m] and L_{trans}=0.0127 [51, p. 299].

The dimensions of the planar numerical domain were specified as (y=10M, z=10M $\approx 20L_{long}$) in order to resemble [59, p. 119]'s 10M preference for their HIT tests. The spatial and temporal resolutions of the domains respectively were $\{64, 128, 256\}_{\mathrm{HIT}}$ node per domain edge, and $\{(0.1, 0.05, 0.025)[t^\star]\}_{\mathrm{HIT}}$, where $t^\star$=$U_cM^{-1}\Delta_t$. The duration of the tests was 10.32[s] $\approx$ 20 pass-through in which each sample contained more than 15000 elements.

[8] For HIT, $\widehat{\beta}_1$ was assumed zero as a consequence of a lack of thoroughly examined data (despite some reports such as $\widehat{\beta}_1 = 0.051$ in [58, p. 310]).

4.1.3. Homogeneous shear turbulence - HST

Towards real-world turbulence, HST could be considered as a transition step wherein large-scale anisotropy is partially incorporated into HIT; nonetheless, the statistical uniformity in space and homogeneity in spanwise direction reduces the sophistication of the flow. By means of HST, isolated effects of *a single* one-spatial-point anisotropic stress and cross-integral length-scale were sought.

The benchmark was the experiment of virtually transverse homogeneous and uniform shear turbulent flow from [60]. The chosen scenario was based on the experimental flow field at a downstream plane of x_1/h=11.0, where h=0.305[m] is the height of the shear-turbulence generator at the experiment inlet, and x_1 the horizontal distance to the generator. At the plane, the mean shear is $\mathrm{dU}_1/\mathrm{d}x_2$=46.8[$\mathrm{s}^{-1}$] and the mean longitudinal flow speed at the plane centreline equals to $\mathrm{U_c}$=12.4[s^{-1}]. Furthermore, Tavoularis and Corrsin [60, p. 321] experimentally found that $\widehat{\beta}_{1x}$=-0.22[2], $\widehat{\beta}_{1y}$=0.16[2], $\widehat{\beta}_{1z}$=0.00, $\widehat{\beta}_{2x}$=0.10, $\widehat{\beta}_{2y}$=0.20 and $\widehat{\beta}_{2z}$=0.30. The random error ranges were $\widehat{\beta}_1 \pm 0.03$[2] and $\widehat{\beta}_2 \pm 0.05$. The input set of stresses and scales contains: $\overline{(u_1')^2}$=0.475[$\mathrm{m}^2\mathrm{s}^{-2}$], $\overline{(u_2')^2}$=0.165, $\overline{(u_3')^2}$=0.248 and $\overline{u_1'\,u_2'}$=-0.126; $\mathrm{L}_{11,1}$=0.057[m], $\mathrm{L}_{22,1}$=0.01311, $\mathrm{L}_{33,1}$=0.01938, $\mathrm{L}_{11,2}$=0.01881, $\mathrm{L}_{11,3}$=0.01425, $\mathrm{L}_{22,2}$=$\mathrm{L}_{22,3}$=0.006555 and $\mathrm{L}_{33,2}$=$\mathrm{L}_{33,3}$=0.00969.[9] [60, p. 320, 329, 334]. The values of the last four scales were derived by employing the isotropy assumption, e.g. $0.5\mathrm{L}_{22,1}$=$\mathrm{L}_{22,2}$.

The dimensions of the domains replicated those of the experiment as (y=h, z=h $\approx$ $7\mathrm{L}_{11,1}$). The spatial resolution of the three grids were: $\{64, 128, 256\}_{\mathrm{HST}}$ node per domain edge, and the corresponding temporal resolutions: $\{(15.6248, 7.8124, 3.9062)[t^\star]\}_{\mathrm{HST}}$, where $t^\star_{\mathrm{HST}}$=$1000\mathrm{U_c}h^{-1}\Delta_t$. The test duration was 7.6864[s], and the samples included at least 40000 elements.

4.1.4. Plane channel flow with smooth walls - PCF

The majority of real-world turbulent flows is bounded by at least one solid surface. Therefore, a fundamental wall-bounded flow, PCF, was utilised to evaluate the capability of the methods in relation to wall effects on flow statistics. In addition, the reconstruction of spatial-variant integral length-scales across flow plane was examined with the aid of PCF.

The benchmark was hinged upon [29]'s direct numerical simulation of statistically stationary, pressure-gradient driven, fully developed plane channel flow with smooth walls, wherein the friction velocity, u_τ, and channel half-width, δ, based Reynolds number is Re_τ=$u_\tau\delta/\nu$=395 [29, p. 943]. The

[9] For $\mathrm{L}_{ij,k}$, ij denote the directions of two velocity components of interest, and k the measurement direction.

input set, including $\widehat{\beta}_1$ and $\widehat{\beta}_2$, is large to show in full herein; for this reason, it can be fetched from the web page of [61] as text files.

The dimensions of the domains were: (y=$2\delta, z$=$\pi\delta$). The spatial and temporal resolutions of the grids were in turn: $\{(64, 100), (128, 201), (256, 402)\}_{\mathrm{PCF}}$ and $\{(8, 4, 2)[t^\star]\}_{\mathrm{PCF}}$, where $t^\star_{\mathrm{PCF}}$=$100\mathrm{U}_c\delta^{-1}\Delta_t$ with the test duration of 25[s] containing at least 200000 elements.

4.2. Statistical measures

The tests were conceptualized into two main branches: *i*. precision tests, wherein the model stages were investigated whether they perform their assigned tasks when they are in isolation, and when they interact each other; and *ii*. accuracy tests, wherein the CFD-free performance of the models in terms of the level of flow reconstruction fidelity was quantified and compared to the test-bed. In §2.1, the model stages were elaborated. For the following plots, the stages were labelled as follows: the incorporation of two-spatial/temporal-point correlation functions: **3$^{\mathbf{rd}}$ stage**, incorporation of one-spatial-point correlations: **4$^{\mathbf{th}}$ stage**, and PDF transformation-based skewness-kurtosis transformation approach: **NG stage**.

The flow reconstructions were explored mainly via six statistical measures: *i*. statistical weak stationarity, *ii*. statistical weak ergodicity, *iii*. first four standardized central moments, *iv*. one-spatial-point correlation tensor of second-order[10], *v*. two-spatial/temporal-point correlation functions, and *vi*. one-dimensional one-sided power spectral density functions. The exact expressions of the measures are summarized in Table 1. In a simulation, each numerical domain node accommodates a time-series of velocity vector. After computing sample statistical measures for the time-series, the measure averages were performed in statistically homogeneous directions. Moreover, whenever suitable, statistics obtained from the test-bed flows and method outcomes were quantitatively compared each other with the help of *discrete Fréchet distance* [62, 63, 64], which is a metric that quantifies the level of similarity between two arbitrary curves. A code from [65, 66, 67] was utilised to compute the metric, which is briefly explained in § Appendix A.4.

4.3. Code practices

In terms of computational cost of DFM/FSM, two model units are the most expensive: *i*. Gaussian random number generation, and *ii*. convolution summation.

[10] The term can also be expressed as *Reynolds stress tensor* when scaled by the density.

The former ideally demands *i*. high computational speed, and samples that are *ii*. statistically independent, and *iii*. fast-convergent to the normal distribution. To that end, in literature, [14] used the central limit theorem wherein $\mathcal{O}(10)$ of uniformly-distributed random number sets are first generated, and then manipulated into Gaussian samples. Later, Touber and Sandham [30, p. 104-105] pointed out that two uniformly-distributed sets are adequate for this purpose if the Box-Muller's theorem is used instead. However, Thomas et al. [68] quantified that the both approaches (and a number of other Gaussian random number generators) could not fulfil the three aforementioned properties satisfactorily and proportionately. The Ziggurat algorithm [69], on the other hand, came to the forefront in their comparisons as the optimum generator [68, p. 5]. Accordingly, in this study, Eddelbuettel [70]'s C++ implementation of a modified Ziggurat algorithm [71] was utilised to generate Gaussian random number sets.

The conventional convolution summation requires FLOPT of $\mathcal{O}\{\left[(\Pi_{m=1}^{i}\mathrm{R}_m)(\Pi_{m=1}^{i}\mathrm{N}_m)\right]_{\{i\in(2,3)\}}\}$.[11] In order to decrease this cost, Veloudis et al. [37, p. 9] reminded first that convolution in the frequency domain is only an element-wise multiplication, thereby the computational time complexity may be reduced by $\mathcal{O}\{\Pi_{m=1}^{i}\mathrm{N}_m/\log\{\Pi_{m=1}^{i}\mathrm{R}_m\}\}$. The following was then proposed for Eq. 2: $\{s\}=\mathscr{F}^{-1}\{\mathscr{F}\{\mathrm{b}\}\mathscr{F}\{\mathrm{r}\}\}$ where $\mathscr{F}$ is a discrete fast Fourier transform operator and $\mathscr{F}^{-1}$ its inverse. Note that $\{\mathrm{b}\}$ is Fourier-transformed only once per simulation. Apart from this proposition, the separable convolution summation method [39, p. 404] was suggested by [38] to evaluate Eq. 2:

$$\begin{aligned}\{s\} = \sum_{k=-\mathrm{N}_p}^{\mathrm{N}_p}\sum_{j=-\mathrm{N}_q}^{\mathrm{N}_q}\sum_{i=-\mathrm{N}_l}^{\mathrm{N}_l}\mathrm{b}_{ijk}\,\mathrm{r}_{m+i,\,n+j,\,o+k} &= \sum_{k=-\mathrm{N}_p}^{\mathrm{N}_p}\sum_{j=-\mathrm{N}_q}^{\mathrm{N}_q}\sum_{i=-\mathrm{N}_l}^{\mathrm{N}_l}\mathrm{l}_i\mathrm{q}_j\mathrm{p}_k\,\mathrm{r}_{m+i,\,n+j,\,o+k} \\ &= \sum_{k=-\mathrm{N}_p}^{\mathrm{N}_p}\mathrm{p}_k\left\{\sum_{j=-\mathrm{N}_q}^{\mathrm{N}_q}\mathrm{q}_j\left[\sum_{i=-\mathrm{N}_l}^{\mathrm{N}_l}\mathrm{l}_i\,\mathrm{r}_{m+i,\,n+j,\,o+k}\right]\right\}\end{aligned} \tag{12}$$

In virtue of this method, the theoretical speed-up becomes in the order of $\mathcal{O}\{\Pi_{m=1}^{i}\mathrm{N}_m/\Sigma_{m=1}^{i}\mathrm{N}_m\}$.[12] The complexity ratio between the Fourier and separable convolutions then turns out to be $\mathcal{O}\{\Sigma_{m=1}^{i}\mathrm{N}_m/\log\{\Pi_{m=1}^{i}\mathrm{R}_m\}\}$. Considering $\mathrm{R}\gg\mathrm{N}$ in DFM, the Fourier convolution is *theoretically* expected to be $\mathcal{O}(1)$-$\mathcal{O}(10)$ faster than the separable convolution. Yet the tests in this study have sug-

[11] For instance, R_2 denotes the size of random set in the 2^{nd}-direction, and N_3 that of the filter coefficient set in the 3^{rd}-direction.

[12] Another method, which has not been utilised in DFM, is the helix transformed [72] convolution, where multi-dimensions are regressed to one-dimension. In tests, however, its cost reduction was observed to be inconsiderable.

gested that the two may deliver considerable and comparable performance gains, likely due to the implementation-algorithm dependent effects.

5. Results & Discussion

In order to avoid duplications, the computation results from all test-bed scenarios were grouped in terms of their common and distinct characteristics. The premises supporting the same argument were presented through representative evidences from one of the benchmarks, and were denoted with a phrase 'representative-to-all' to make clear when the concluding remarks are valid for all scenarios. Furthermore, the spatio-temporally grid independent results were reported, which belong to the following numerical domains: $\{64\}_{\mathrm{HIT}}$, $\{64\}_{\mathrm{HST}}$ and $\{64, 100\}_{\mathrm{PCF}}$ node per domain edge.

5.1. The first four one-spatial-point statistical moments

The 4^{th} model stage requires that the sets of the 3^{rd} stage output, $\{s\}$ of Eq. 2, has zero-mean and unit-variance [13, p. 656]. The majority of the literature presumes that the requirement is automatically fulfilled. Veloudis et al. [37, p. 8-9], however, held an opposite view that the 3^{rd} stage generally alters the zero-mean unit-variance of the random number sets. Therefore, they proposed a renormalization of $\{s\}$ to ensure the requirement is fulfilled.[13] The authors nevertheless did not present any quantification to support this objection.

To assess the view, the sample mean and sample standard deviation of each node-time-series were computed at each stage of the models. Further, the arithmetic average and variance of all these sample pairs were calculated. Table 3 presents a *representative-to-all* HIT results for this quantification. Data in the table shows that the order of magnitude of changes in zero-mean and unit-variance due to the 3^{rd} stage is around 0.001 with a variance of around 0.0001. The effect of the non-Gaussian stage is, on the other hand, several decades lower than that of the 3^{rd} stage. Moreover, the observation is consistent across DFM/FSM methods. Contrary to [37]'s argument, the study did not find a significant effect of the 3^{rd} (as well as the non-Gaussian) stage on the zero-mean and unit-variance. In addition, the low variance indicated the level of effect is almost the same across stochastically and statistically different node-time-series. The renormalization requires operations of an addition, a summation, an exponentiation and a square-root per grid-node at each

[13] As an example, [38, p. 59] used the renormalization.

time-step. More importantly, the time-series throughout the duration of a computation needs to be known a priori, because time averages should be performed for the normalization. This may demand large data storage and complicate on-the-fly computations. It is thus suggested that the renormalization is redundant in terms of its effects, and its omission is advisable to avoid extra cost and complications.

Following the first two moments, the skewness-kurtosis pairs of the benchmarks were reconstructed through the new PDF transformation-based approach, Eq. 11. Fig. 3 and 4 illustrate *representative-to-all* PCF skewness and kurtosis results, respectively.

In the both figures, the 3$^{\text{rd}}$ stage's skewness-kurtosis pairs closely follow the values of (0–3). This confirms that the pairs produced by the original DFM/FSM is Gaussian. This also corroborates the presumption that the input set of statistics as it stands does not automatically develop higher-order moments during the flow reconstruction. By contrast, as shown in the figures, the new non-Gaussian stage helped DFM/FSM to closely reconstruct the skewness-kurtosis pairs of the benchmark in terms of magnitude and patterns despite their spatial variation across a considerable range of pair combinations. Additionally, in the non-Gaussian stage, no appreciable differences were observed among DFM/FSM methods. This finding implies that the different 3$^{\text{rd}}$ stages of the methods do not affect the subsequent non-Gaussian stage outcomes.

The 4$^{\text{th}}$ stage needs a closer look, because [20, p. 96] put forward the idea without quantification that this stage, Eq. 3, alters the statistics constructed in the previous stages. The reasons and extent of the alterations were however not examined therein as well as in the literature. Fig. 3 and 4 may provide some insights into the argument.

In fact, the v-component skewness-kurtosis pairs were observed distorted by the 4$^{\text{th}}$ stage. The maximum change due to the 4$^{\text{th}}$ stage in skewness was around 10% and in kurtosis 5%.[14] The level of distortion was gradually increased with the distance to the Gaussian values; nevertheless, the overall benchmark pattern was preserved in the numerical results. What's more, the asymmetry of the distortion for the same v-skewness magnitudes at different channel heights implied that the magnitude of skewness-kurtosis pairs and Reynolds stress tensor components determine the distortion level in a nonlinear interrelation.

[14] Percentage difference=$(x_r\text{-}x_n)/x_r \cdot 100\%$, where x_r is the magnitude of the relevant parameter for the reference, and x_n that for the numerical study.

On the contrary, no 4^{th} stage effect was found on the skewness-kurtosis of u-,w-components. This discrepancy stems from Eq. 3. In the 4^{th} stage, the amplitude of $\{s^u\}$-sets is solely multiplied element-wise by time-invariant a_{11} whereas the operation adopted for $\{s^v\}$-sets includes a multiplication and an addition: i.e. $v{=}s^u\,a_{21}{+}s^v\,a_{22}$. In the former, the sole multiplication causes the same scaling at two separate points of $\{s^u\}$-sets in space and time, thereby the two-point correlation functions as well as one-point moments of the sets remain unchanged. In the latter, however, the addition of a stochastic $\{s^u\}$-set distorts the amplitude proportionality between any two-spatial/temporal points within a $\{s^v\}$-set; hence, distortion in embedded statistics. This disruption should also be detected for w-component while its 4^{th} stage consists of three multiplication and two additions: i.e. $w{=}s^u\,a_{31}{+}s^v a_{32}{+}s^w\,a_{33}$. The disruption was however absent for PCF because the additions vanish due to the statistical homogeneity in the w-direction: $a_{31}{=}a_{32}{=}0$.

Furthermore, the same patterns were observed for HST as can be seen from Table 5 wherein only v-component skewness-kurtosis differed in nearly (18-2)% compared to the previous stage. Considering this explanation, the 4^{th} stage should have no effect on the pre-embedded statistics for HIT, because the absence of any one-point cross-correlation component should eliminate all the addition operations. Indeed, Table 4 confirms this expectation as all the skewness-kurtosis pairs remained the *same* at the end of the 4^{th} stage.

These findings suggest that the 4^{th} stage, namely the Lund transformation, to some extent distorts the pre-existing statistics only in the statistically inhomogeneous lateral directions. On the other hand, the same findings indicate that the streamwise and statistically homogeneous lateral direction statistics are not prone to such distortion.

5.2. One-spatial-point second-order correlation tensor

The reconstruction of the one-spatial-point second-order correlation tensor of fluctuations (hereafter, the tensor) is fundamental to the synthetic turbulence generation, because the evolution of turbulence mostly depends upon energy transfer processes shaped by the tensor. The gradients of the mean velocity components work done on the deviatoric part of the tensor. This part then energizes the isotropic part of the tensor (whose half trace is the turbulent kinetic energy) which redistributes and dissipates the energy. As a result, the mean velocity field loses its convective momentum to the fluctuating velocity field. A realistic turbulence development therefore demands successful reconstruction of the tensor.

Fig. 5 presents the *representative-to-all* PCF results for the six tensor components[15] reconstructed by the 4$^{\text{th}}$ model stage. Due to the antisymmetry of the deviatoric tensor around the channel half-height, the results across the entire section were shown. As a consequence of inadequate spatial resolution adjacent to the walls, numerical results for a few benchmark points were not available in the figure.

The results demonstrate that spatial-variant fields of the reconstructed tensor components were virtually the same with the benchmark. For instance, the maximum deviation among all scenarios was observed 3.8% away from the benchmark, which belongs to Kim et al.'s construction of $\overline{w'\,w'}^{+}$ near the top wall. In comparison to the rest of the results, however, this deviation could be considered an outlier whilst the majority of all deviations was found to be below 1%. Furthermore, apart from minor differences because of the stochastic nature of model outcomes, no significant difference among models, including non-Gaussian counterparts, was identified. The most likely reason of this is that each model used the same Lund transformation for the 4$^{\text{th}}$ stage, and this stage was followed by no other model stage. Another implication of this indifference is that the previous model stages do not have any appreciable effect on the 4$^{\text{th}}$ stage output. Lastly, $\overline{u'\,w'}^{+}$ and $\overline{v'\,w'}^{+}$ subplots in Fig. 5 illustrate an evidence for the presumption that the level of reconstruction of DFM/FSM is restricted by the input statistics while no input was provided for the both components due to the statistical homogeneity in the spanwise direction of the flow, and indeed, the both correlations remained random.

5.3. Two-spatial/temporal-point correlation functions

In this section, *representative-to-all* results of the variance-normalized two-spatial/temporal-point sample autocorrelation functions (hereafter, autocorrelation) are presented with three figures in order to examine primarily patterns and similarities. First, Fig. 6 and 7 show the results obtained from HIT and HST computations. The two includes two longitudinal, $\widehat{\rho}_{\mathbf{xu}}$ and $\widehat{\rho}_{\mathbf{yv}}$, and one lateral autocorrelation, $\widehat{\rho}_{\mathbf{xv}}$, in order to additionally discuss the DFM/FSM model stage effects on the autocorrelation. Second, Fig. 8 exemplifies a complete autocorrelation tensor from HST computations to fill the gap that the majority of studies in the literature contended with in reporting longitudinal autocorrelations only, e.g. $\widehat{\rho}_{\mathbf{xx}}$ or $\widehat{\rho}_{\mathbf{yy}}$.

[15] The tensor is symmetric.

To begin with, no noticeable alterations due to the non-Gaussian stage were found. The remark is exemplified in Fig. 6 and 7 where the non-Gaussian stage outcome bears a marked resemblance to the previous 3$^{\text{rd}}$ stage. This is also valid for PCF computations wherein the skewness-kurtosis pairs are highly varying, and is supported by §5.2 observations. Secondly, as can be deduced from Fig. 6, no change due to the 4$^{\text{th}}$ stage took place in HIT whereas Fig. 7 reveals that the Lund transformation caused a rise nearly 10% of the zero-lag in the most $\widehat{\rho}_{\mathbf{xv}}$ and $\widehat{\rho}_{\mathbf{yv}}$ of HST. On the other hand, $\widehat{\rho}_{\mathbf{xu}}$ of HST was found to be unaltered. These results are in agreement with those obtained in §5.1, which further support the aforementioned three remarks: *i*. in the absence of anisotropic Reynolds stresses, the 4$^{\text{th}}$ stage does not adversely affect the previous stage statistics, *ii*. in the presence of anisotropic Reynolds stresses, the 4$^{\text{th}}$ stage remains neutral to the pre-existing statistics in the streamwise and statistically homogeneous lateral directions; however, *iii*. the 4$^{\text{th}}$ stage amplifies those statistics in the statistically inhomogeneous lateral direction, which almost certainly leads to an uninvited increase of output turbulence scales in this direction.

On the question of similarities, the following observations were made. According to the Fréchet distance in the horizontal bar charts of the figures, the closest and farthest overall proximity to the reference autocorrelation tensor components were yielded by the Custom and Klein et al.'s methods, respectively, with no counter-examples. In addition, Kim et al.'s method nearly always produced the second best approximations, which also closely followed the Custom's high fidelity reproductions. Xie-Castro's method mostly ranked number three; nevertheless, occasionally reached Kim et al.'s fidelity. With respect to the patterns in the output autocorrelations, five patterns were observed. *i*. One finding is that Klein et al.'s method produced Gaussian-shaped autocorrelations although the rest of the models as well as the benchmarks yielded exponential forms. This confirms the anticipation that the filter kernel casts whatever its shape onto the output autocorrelations. Another implication of the finding is that the Gaussian-form is not an appropriate choice for the benchmark flows considered, and very probably also, not for the other turbulent flows which share similarities with these three benchmarks. The remaining four patterns are *maximal* generalizations about the performance of the models, because they were observed consistently across different flow scenarios: *ii*. Klein et al.'s method overpredicted the references by $\sim$20-25 $\pm$ 5% up to $\sim$20-25% of the zero-lag, and then underpredicted them by $\sim$10%. *iii*. By contrast, the Custom method generally reconstructed the references with less than $\sim$1% difference. Yet its 4$^{\text{th}}$ stage resulted in $\mathcal{O}(1)$% increase in autocorrelations of the statistically inhomogeneous lateral direction, e.g. $\widehat{\rho}_{\mathbf{xv}}$

of HST. *iv*. Similarly, Kim et al.'s method reproduced the references in close resemblance up to ∼20% of the zero-lag, and then slightly underpredicted them with few exceptions, e.g. $\widehat{\rho}_{\mathbf{zu}}$ of HST. *v*. Lastly, Xie-Castro's method usually resulted in ∼5-10% overpredictions along the most part of the benchmark autocorrelations. In some of the cases, however, the method made a higher overprediction around ∼20-25% till ∼15-20% of the zero-lag, which was followed by an underprediction, as can be seen in $\widehat{\rho}_{\mathbf{zw}}$ of HST. Considering these results, the overprediction tendency could conceivably be hypothesised that DFM/FSM as is often greatens input scales to some extent.

Another subtle finding was about the streamwise autocorrelations of PCF, which do not level off zero, yet a positive constant value. It was observed that DFM/FSM could not construct such tail behaviour, because their theoretical equations decay *certainly* and asymptotically to zero at a certain decorrelation distance.

5.4. Power spectral density functions

This section presents *representative-to-all* results of the sample one-dimensional one-sided power spectral density functions as a function of spatial wavenumbers (hereafter, power spectrum) in order to investigate the model stage effects and performance of the models within inertial and energy containing ranges of the spectrum. Representative evidence of the following remarks are illustrated in Fig. 9 and 10 respectively for HIT and HST.

What stands out in the both figures is a premature and flow-type-independent drop with a non-linear slope in the power spectra created by Klein et al.'s method towards the outset of inertial range wavenumbers. Klein et al. [13] did not report any result for power spectra; however, [59, p. 122] identified a similar drop for this method in HIT. The most likely cause of the drop is the method's Gaussian-form of the filter function. Consider the Fourier transform of the Gaussian autocorrelation function, Eq. 4, whose derivation and parametrization are given in Appendix A.5.1 [73]:

$$\mathscr{F}_x \left\{ \exp\left[-\frac{\pi}{4} \frac{x^2}{\mathrm{L}^2} \right] \right\} (\kappa) = 2\,\mathrm{L}\, \exp\left[-4\pi \mathrm{L}^2 \kappa^2 \right] \tag{13}$$

which is also another Gaussian function, where $\mathscr{F}_x$ is the Fourier transform operator on the spatial variable $\{x\}_{\{x>0\}}$, $\mathrm{L}\,[\mathrm{m}(2\pi)^{-1}]$ an integral length-scale, and $\kappa\,[(2\pi)\mathrm{m}^{-1}]$ the spatial wavenumber. Eq. 13 in Fig. 9 and 10 illustrates that Klein et al.'s method theoretically produces the drop. Herewith the model, towards the inertial range, the power spectrum declines considerably more

rapidly than $\kappa^{-5/3}$. Consequently the net spectral energy flux in the inertial range also steeply decreases; thus, leading to a spurious preservation of the energy in large scales along time.

In contrast, two different observations were noted in Fig. 9 and 10 for all the other methods' inertial range reconstructions: first, the aforementioned drop disappeared and the inertial range slope was more closely followed; and second, an upward transient spike occurred at the high-wavenumber tail. As regards the power spike, temporal aliasing can be attributed as the main contributor to this excess power, which typically results from the sampling process rather than the models. Therefore, no further explanation was sought for the second observation.

One of the major differences between Klein et al.'s method and the rest is that the autocorrelation function of the latter has an exponential-form. The *Gaussian-exponential* distinction might be the key factor in the power drop formation. In order to examine this postulation, a Fourier analysis likewise above was performed for the exponential function. In addition, Klein et al.'s Gaussian-form was converted into an exponential one, and several tests were carried out. The Fourier transform of the exponential autocorrelation function, Eq. 7, can be shown as follows (Appendix A.5.2 [74]):

$$\mathscr{F}_x \left\{ \exp\left[-\frac{\pi}{4} \frac{x}{\mathrm{L}} \right] \right\} (\kappa) = \frac{8\mathrm{L}\pi^{-1}}{(8\mathrm{L}\kappa)^2 + 1} \tag{14}$$

which is a Lorentzian function that theoretically possesses a linear decay slope of κ^{-2} after a corner wavenumber, κ_c. Accordingly, Eq. 14 was also plotted in Fig. 9 and 10.

Inspection of the two figures reveals a number of characteristics. First, the Fréchet distances of the 4^{th} stage and qualitative examination indicate that the Custom, Kim et al. and Xie-Castro's methods performed alike in overall spectra estimation unlike the both Klein et al.'s methods. Yet the energy-containing range patterns were adequately estimated by all the methods, both Gaussian- and exponential-form; thus, no superiority of one form on the other in this respect. Another observation comparing the 3^{rd} and 4^{th} stages is that the overall shape of the power spectra is established by the 3^{rd} stage only whilst the 4^{th} stage seems responsible in rescaling the power level to the target. In addition to this, the non-Gaussian stages shown in Fig. 9 and 10 assert that the skewness-kurtosis transformation did not modify the power spectra previously constructed in the 3^{rd} stage.

A closer look into the inertial subrange of the both figures' 3^{rd} stages discloses that the inertial subrange slopes created by the exponential-form methods (except the exponential Klein et al.'s method) and the corresponding Lorentzian functions are virtually the same. The power amplitude of

these methods are, however, generally $\sim \mathcal{O}(1)$ order of magnitude higher than that of the Lorentzian functions.

The implications of these findings are threefold. First of all, the exponential-form methods seem to yield the inertial subrange slope of κ^{-2}=$\kappa^{-6/3}$ rather than $\kappa^{-5/3}$. The former's slope is still steeper than that of the latter albeit to a significantly lesser extent than by Eq. 13. Because of this, the above-mentioned decrease of the net spectral energy flux generated by the Gaussian-form methods continues its existence, yet with a significantly reduced dissimilarity to what $\kappa^{-5/3}$ may produce. Further quantifications may however be needed whether this level of difference between κ^{-2} and $\kappa^{-5/3}$ is negligible from the perspective of turbulence development. Second, the use of Eq. 14 as well as 13, which were parametrized for DFM/FSM herein for the first time, could be useful in order for predicting power spectra of a prospective simulation before actually completing the entire simulation.

Thirdly, the exponentiality incorporated into Klein et al.'s method eliminated the Gaussian power drop *to a large extent*; however, a slight decline persisted in the order of $\sim \mathcal{O}(1)$-$\mathcal{O}(10)$ with respect to the other exponential-form methods. Furthermore, the method's slope was found considerably flatter than those of Gaussian-form methods, yet mildly steeper than κ^{-2}. This outcome is somewhat counterintuitive, because the implementation of the exponential-form was expected to transform Klein et al.'s method into an exponential-form method in all aspects. Accordingly, the results imply that the omission of Gaussian-form correlation function, per se, is the key to avoid the aforestated spurious power drop whereas another unnamed mechanism within Klein et al.'s method also seems to contribute the drop.

It should be highlighted that similar observations were also deduced for PCF and different spectra, e.g. $\widehat{\mathrm{E}}_{\mathbf{vv}}$. In summary, these deductions support the notion that exponential-form of correlations is more apt than Gaussian-form for the synthetic turbulence generation.

5.5. Miscellaneous

5.5.1. Statistical weak stationarity and ergodicity

The initial presumption of the model development for DFM/FSM is the *statistical weak stationarity* of time-series generated by each model stage. The augmented Dickey-Fuller unit-root test [75], which searches stochastic trends in a time-series, was used to quantify the stationarity. As a result, *all* velocity-component time-series from each stage of each benchmark, including skewness-

kurtosis computations, were found to be statistically weak stationary at a 1% statistical significance level.

The second presumption is the *statistical weak ergodicity* of the time-series. The Walf-Wolfowitz test [76] was utilised to assess the ergodicity. The test requires two samples of the same size from the same method, e.g. containing $n \times m$ elements. The first sample is generated with a single random seed which initializes the pseudorandom number generator. The second sample is then generated as a combination of n subsamples containing m elements, where each subsample is created with a new random seed. For a given moment of order k, the test conducts comparisons for whether the invariance of the k^{th} moment's statistics is preserved in spite of the stochastic differences in the samples. Grazzini [76, p. 7] suggests n=100 and m=1000 for a decent estimation. With this suggestion, the test was performed for all the 36 benchmark/model scenarios up to the first four central moments of each velocity component. At a 5% statistical significance level, 9 out of 144 cases were estimated non-ergodic. No clear pattern was observed among the non-ergodic cases; however, 4 of them belonged to kurtosis. Owing to the high portion of the ergodic cases, it can be concluded that DFM/FSM is almost always *weakly ergodic* up to the fourth moment. In consequence, a stationary sample from DFM/FSM almost certainly includes the true moments of the population.

5.5.2. The use of different correlation functions at inlet spatial zones

In the literature, DFM/FSM has almost always been utilised by using a single set of integral length- or time-scales as an input for an entire synthetic turbulence generation plane. Two deficiencies may arise from this practice. First, in reality, length- and time-scales may spatiotemporally vary across a typical cross-section of a flow. Second, the usage of a single set of time-scales inherently causes a spatial variation in particularly streamwise length-scales due to the Taylor's frozen turbulence hypothesis [40] unless cross-sectional mean flow speed is uniform. For example, two pockets of fluctuation generated with the same time-scale and at two different spatial positions will convect downstream proportional to the convective mean longitudinal flow speed at these two points. If these flow speeds differ from those considered in the time-scale computation, the corresponding length-scales will be different to each other. Moreover, the literature preference for the single set usage seems due to the lack of not only available data but also quantifications regarding the merits and costs of using more-than-one sets as an input.

In this part, therefore, effects of the spatial variation in turbulence scales are investigated.

To this end, PCF was reconstructed by using a single and then twelve sets of integral length-scales (tagged by **1L** and **12L** in the figures, respectively). Comparisons for correlations and power spectra were made, and *representative-to-all* results were presented. For the **12L** case, the synthetic turbulence generation plane was geometrically divided into twelve zones in the wall-normal direction. The zonal dimensions and associated correlation functions were provided by the benchmark. The integral length-scales were computed through the integration of these correlation functions, where the upper bound of the integration was set to 10% of the zero-lag.[16] Each input set of each zone contained nine integral length-scales belonging to each velocity component-direction pair, (u, v, w)-(x, y, z). For the **1L** case, the length-scales reported for the channel half-height, y^+=392, were input uniformly across the generation plane.

Fig. 11 and 12 shows the *representative-to-all* results of the variance-normalized sample auto-correlation function, $\widehat{\rho}_{\mathbf{xu}}$, as a function of spatial lag for **1L** and **12L**, in turn. Each figure includes twelve subplots related to a zone whose centre is at a vertical distance of y^+ from the wall.

In Fig. 11, the first observation is that the use of **1L** produced a variation in streamwise length-scales across the channel cross-section, increasing from the wall to the channel centreline. This is due to the fact that the **1L** length-scales was converted to Lagrangian time-scales based upon the mean flow speed at the height of y^+=392 through the Taylor's hypothesis. In a constant time-step computation, however, inputting the same Lagrangian time-scales across the channel cross-section automatically caused variations of length-scales because of the spatial varying mean flow speed across the same section. Consequently, this gave rise to uncontrolled generation of different scales. In addition, the following patterns were deduced from Fig. 11. Underpredictions occurred in all y^+ zones and for all methods after a certain percentage of the zero-lag. In y^+=10 zone, the common underprediction started at $\sim$ 90% zero-lag. Towards higher y^+ zones, this starting point then reduced till $\sim$ 40-70% zero-lag with gradually decreasing slope. Typically, Klein et al.'s method yielded maximum $\sim$ 20-30% underpredicted correlations whereas this ratio remained around $\sim$ 5-15% for the other methods. On the other hand, in y^+=392 zone where the input **1L** belongs to,

[16] The integral length-scale, L, is defined here as follows: $\mathrm{L}=\mathscr{L}_0^{\infty}(\widehat{\rho}(\Delta)) \approx \mathscr{L}_0^{a}(\widehat{\rho}(\Delta))$, where $\mathscr{L}_b^{a}(\cdot)$ is an operator applying a numerical integration method over the interval $[a, b]$. Despite its precise definition, the upper bound of the integral, i.e. b, is open to debate. Arguably, the main reason of the doubt is the different interpretations of the tail of the correlation functions on whether their tails mean something physical or spurious. Nicolaides et al. [77, p. 3] implied based upon several tests that selecting the upper bound when the first zero-crossing happens is the most convenient option. This was, however, found inappropriate for the PCF while particularly the streamwise correlations do not level off zero.

the method performance findings in §5.3 were reobserved.

In Fig. 12, the observations similar to in §5.3 spread out the other y^+ zones by virtue of the spatial variation. On the whole, as maxima, Klein et al.'s method made $\sim$ 20-40% overpredictions until $\sim$ 20% zero-lag and afterwards $\sim$ 20% underpredictions. Xie-Castro's method overpredicted the benchmark in the level of $\sim$ 5-20% without exception. Custom and Kim et al.'s methods followed the benchmark in high proximity except in the y^+=251 zone[17], yet the latter deviated for $\sim$ 5-10% underpredictions after $\sim$ 20% zero-lag.

Fig. 13 and 14 compared the power spectra for the **1L** and **12L** cases. As Fig. 13 shows, Klein et al.'s method yielded the aforementioned power drop except for the y^+=10 zone where the model outcome seems comparable to the benchmark. The rest of the methods performed in a common trend wherein the level of similarity to the benchmark was improved till y^+=61, then stayed roughly the same until y^+=151, and fell off. In detail, these methods had $\sim\mathcal{O}(10^3\text{-}10^4)$ higher power with respect to the spectrum tail at the y^+=10 zone. The difference steadily reduced to $\sim\mathcal{O}(10^2)$ by the y^+=61 zone and remained almost unchanged until y^+=151. Subsequently, it rose back to $\sim\mathcal{O}(10^3)$ towards the channel centreline.

As illustrated in Fig. 14, the performance trend of the models in Fig. 13 was repeated yet with a reduced degree of differences to the benchmark overall. Unlike the y^+=10 zone resemblance of Klein et al.'s method in the **1L** case, the likeness disappeared in the **12L** case with the refined length-scale input therein. That resemblance therefore may seem now to be a mere coincidence. The degree of the power difference, with respect to the spectra tails, overpredicted by the rest of the models was $\sim\mathcal{O}(10^2\text{-}10^3)$, $\sim\mathcal{O}(10^1\text{-}10^2)$ and $\sim\mathcal{O}(10^2\text{-}10^3)$ for the sectors between y^+=10-61, y^+=61-151 and y^+=151-392, respectively.

Taken together, the results of this section indicate that the spatial variation of scales often improves the overall statistical fidelity till the natural boundaries of fidelity that a model provides. In a single set of scales case, in contrast, somewhat arbitrary and hard-to-control statistics form in terms of magnitude and patterns for the majority of regions of a flow.

The spatial variation of scales brings along some theoretical and practical shortcomings, nevertheless, which are distinct for DFM and FSM. Klein et al. [13, p. 658] discouraged the use of

[17] It should be mentioned that the main reason why the discrepancy from the Custom method at the y^+=251 zone occurred could not be spotted and explained.

the spatial variation of length-scales in DFM. The authors foresaw that such practice almost surely causes two issues: *i*. the Gaussian-form of Eq. 4 is distorted, and *ii*. an essential building-block assumption for the derivation of Eq. 1 is violated. Klein et al. [13], however, saw the spatial variation from another angle. The authors expected the acquisition of the variation occurs through calibrating filter coefficients within a single filter in accordance to given spatial-variant length-scales, namely via a *spatially varying filter*, and filtering an *undivided* synthetic turbulence generation plane with this filter. This, in fact, violates the essential model assumption wherein the filter coefficients were assumed spatially constant.

In the current DFM approach, however, the generation plane is separated into zones, and different *spatially-invariant* filters are put to use at different zones. Accordingly, each zone independently possesses associated scales without breaching the two above-mentioned issues. Although the zone-separation discards these two theoretical issues, this approach suffers from two new practical weaknesses. Firstly, statistical discontinuities emerge between zone boundaries. In particular, the statistics in the zone-separation direction are more prone to such discontinuities. As an example, the size of a zonal scale may far exceed the dimension of its zone. While non-CFD applications might not be adversely affected as zones remain independent of each other, CFD applications could be profoundly influenced by unforeseen impacts on turbulence evolution due to the nonlinear mixing of discontinuities downstream.

In the limit of infinite grid nodes and zones, prospective discontinuities may disappear. The second weakness, however, arose as a limiting factor is the extra computational cost. Veloudis et al. [37, p. 9] stated without an explanation or quantification that a modest increase in the number of zones results in a 'substantial' cost increase for the same number of nodes. The reason why the cost increases is two-fold: *i*. new $\sim k(x\text{-}1)(\text{N-}1)$ random numbers required to be generated per time-step, where k is the number of scales input into a zone, x the number of zones, and N the filter support for a scale (Appendix A.6), and *ii*. these new numbers increase the size of sets which need to be convolved each time-step. Taking into these account, the additional computational cost is estimated by $\mathcal{O}(1)$ times the current cost.

The above remarks are pertinent to only DFM. FSM is immune to such cost impact. The zone-separation is not demanded by FSM, and the spatial variation is achieved through *solely* a spatial-variant arrangement of the input scale set. In this regard, a possible problem for FSM *may* be that the derivation of Eq. 8 for the spatial variation of scales was not engaged with by the

literature, to date.

Notwithstanding these concerns, the results obtained in practice arguably weigh the merits of the spatial variation of scales more against additional costs. As an outcome, such implementation is advisable for non-CFD applications, particularly for FSM because of the fact that it poses considerably less trouble to beneficiaries.

6. Conclusions

The main aim of this study was to provide beneficiaries quantitative insights regarding the working mechanisms and performance of digital-filter-based (DFM) and forward-stepwise-based (FSM) synthetic turbulence generation methods. Another aim of the study was to add them a capability wherein one-spatial-point skewness and kurtosis values can be changed to target values.

To this end, four synthetic turbulence generation methods that belong to Kim et al. [35] (FSM), Xie-Castro [14] (Hybrid DFM-FSM), Klein et al. [13] (DFM), and a new method (DFM) were implemented into OpenFOAMv1612+. The novel applications within the methods were twofold: First, the new method, named *Custom*, was developed as a more efficient version of di Mare et al.'s concept [18]. Second, Kim et al.'s method was formalized and put through its first major tests. In addition to these, a new, cheap-to-run and easy-to-code piecewise closed-form function that transforms one-spatial-point Gaussian skewness-kurtosis of a given time-series to a non-Gaussian pair was derived from a combination of the memoryless nonlinear transformation method and the Johnson system of probability distribution functions. All the methods were abstracted into four modelling stages. Prior to transfer the model outputs into CFD simulations, the methods were explored in isolation via a test-bed containing decaying homogeneous isotropic turbulence, homogeneous shear turbulence and smooth-wall plane channel flow by means of various statistical measures and aspects.

In conclusion, apart from minor findings stated within the text, the study provided six primary insights: (*i*). the new non-Gaussian functionality successfully embeds target one-spatial-point skewness-kurtosis pairs into synthetic turbulence time-series, and does not alter the other types of existing statistics within the series. (*ii*). Moreover, the Lund transformation does not alter previous model stage statistics when anisotropic Reynolds stresses are absent. However, on the condition that anisotropic stresses are present, the Lund transformation amplifies the existing statistics *only* in statistically inhomogeneous lateral directions. The amplification generally manifests itself as a

maximum ∼10% increase in autocorrelation functions. Statistics in the streamwise and statistically homogeneous lateral directions are, on the other hand, not affected by the transformation in contrast to the presumption in the literature. (*iii*). The level of reconstruction fidelity in terms of autocorrelation functions and power spectra was obtained by the methods of, which are sorted from the highest to the lowest level: Custom, Kim et al., Xie-Castro and Klein et al.. (*iv*). Kim et al.'s method provides the best trade-off between the reconstruction fidelity and computational cost. (*v*). Correlation functions determine overall shape of their power spectra. In detail, all methods reconstruct energy-containing region of the spectra in high fidelity. Yet Klein et al.'s method theoretically and numerically produces a premature and flow-type-independent Gaussian drop in power spectra towards wavenumbers higher than those of energy-containing region, predominantly due to its Gaussian-form of correlation functions. In contrast, the rest of the methods, which uses exponential-form correlation functions, yields $\sim\kappa^{-2}$-slope drop by theoretical and numerical means. (*vi*). The spatial variation of correlation functions at a turbulence generation plane through zones was found to increase the overall fidelity of autocorrelation functions and power spectra. Its merits weigh more than its accompanied costs, particularly for FSM.

Last but not least, further research is required to determine whether the findings of the study differ within CFD simulations. For this purpose, the transfer and evolution of DFM/FSM output inside CFD simulations need to be quantified systematically.

7. Acknowledgement

The authors acknowledge the use of the IRIDIS High Performance Computing Facility, associated support services at the University of Southampton, in the completion of this work. Bercin also acknowledges the international research studentship from the Faculty of Engineering and the Environment at the University of Southampton.

References

References

[1] C. Rosales, C. Meneveau, Anomalous scaling and intermittency in three-dimensional synthetic turbulence, Physical Review E 78 (1) (2008) 016313. doi:10.1103/PhysRevE.78.016313.

[2] S. AL-Bairmani, Y. Li, C. Rosales, Z.-T. Xie, Subgrid-scale stresses and scalar fluxes constructed by the multi-scale turnover Lagrangian map, Physics of Fluids 29 (4) (2017) 045103. doi:10.1063/1.4979719.

[3] K. Gong, X. Chen, Influence of non-Gaussian wind characteristics on wind turbine extreme response, Engineering Structures 59 (2014) 727–744. doi:10.1016/j.engstruct.2013.11.029.

[4] J. Berg, A. Natarajan, J. Mann, E. G. Patton, Gaussian vs non-Gaussian turbulence: impact on wind turbine loads, Wind Energy 19 (11) (2016) 1975–1989. doi:10.1002/we.1963.

[5] N. S. Dhamankar, G. A. Blaisdell, A. S. Lyrintzis, Overview of turbulent inflow boundary conditions for large-eddy simulations, AIAA Journal (2017) 1–18doi:10.2514/1.J055528.

[6] G. R. Tabor, M. H. Baba-Ahmadi, Inlet conditions for large eddy simulation: A review, Computers and Fluids 39 (4) (2010) 553–567. doi:10.1016/j.compfluid.2009.10.007.

[7] X. Wu, Inflow turbulence generation methods, Annual Review of Fluid Mechanics 49 (1) (2017) 23–49. doi:10.1146/annurev-fluid-010816-060322.

[8] J. Mann, Spectral velocity tensor in moderately complex terrain, Journal of Wind Engineering and Industrial Aerodynamics 88 (2-3) (2000) 153–169. doi:10.1016/S0167-6105(00)00046-5.

[9] R. H. Kraichnan, Diffusion by a random velocity field, Physics of Fluids 13 (1) (1970) 22. arXiv:arXiv:1011.1669v3, doi:10.1063/1.1692799.

[10] S. Lee, S. K. Lele, P. Moin, Simulation of spatially evolving turbulence and the applicability of Taylor's hypothesis in compressible flow, Physics of Fluids A 4 (7) (1992) 1521–1530. doi:10.1063/1.858425.

[11] P. Druault, S. Lardeau, J.-P. Bonnet, F. Coiffet, J. Delville, E. Lamballais, J.-F. Largeau, L. Perret, Generation of three-dimensional turbulent inlet conditions for large-eddy simulation, AIAA Journal 42 (3) (2004) 447–456. doi:10.2514/1.3946.

[12] N. Jarrin, S. Benhamadouche, D. Laurence, R. Prosser, A synthetic-eddy-method for generating inflow conditions for large-eddy simulations, International Journal of Heat and Fluid Flow 27 (4) (2006) 585–593. doi:10.1016/j.ijheatfluidflow.2006.02.006.

[13] M. Klein, A. Sadiki, J. Janicka, A digital filter based generation of inflow data for spatially developing direct numerical or large eddy simulations, Journal of Computational Physics 186 (2) (2003) 652–665. doi:10.1016/S0021-9991(03)00090-1.

[14] Z. T. Xie, I. P. Castro, Efficient generation of inflow conditions for large eddy simulation of street-scale flows, Flow, Turbulence and Combustion 81 (3) (2008) 449–470. doi:10.1007/s10494-008-9151-5.

[15] L. E. Borgman, Ocean wave simulation for engineering design, Technical report, Hydraulic Engineering Laboratory, Berkeley, California (1967).

[16] H. Nobach, Verarbeitung stochastisch abgetasteter signale, Ph.d. thesis, University of Rostock, Germany (1997).

[17] T. S. Lund, X. Wu, K. D. Squires, Generation of turbulent inflow data for spatially-developing boundary layer simulations, Journal of Computational Physics 140 (2) (1998) 233–258. doi:10.1006/jcph.1998.5882.

[18] L. di Mare, M. Klein, W. P. Jones, J. Janicka, Synthetic turbulence inflow conditions for large-eddy simulation, Physics of Fluids 18 (2) (2006) 025107. doi:10.1063/1.2130744.

[19] L. di Mare, W. P. Jones, Algebraic and operator methods for generation of inflow data for LES and DNS, in: Fourth International Symposium on Turbulence and Shear Flow Phenomena (TSFP4), Williamsburg, Virginia, 2005, pp. 687–692.

[20] M. Fathali, M. Klein, T. Broeckhoven, C. Lacor, M. Baelmans, Generation of turbulent inflow and initial conditions based on multi-correlated random fields, International Journal for Numerical Methods in Fluids 57 (1) (2008) 93–117. doi:10.1002/fld.1627.

[21] A. Kempf, M. Klein, J. Janicka, Efficient generation of initial- and inflow-conditions for transient turbulent flows in arbitrary geometries, Flow, Turbulence and Combustion 74 (1) (2005) 67–84. doi:10.1007/s10494-005-3140-8.

[22] G. Fru, G. Janiga, D. Thévenin, Direct numerical simulation of highly turbulent premixed flames burning methane, in: H. Kuerten (Ed.), ERCOFTAC Series, Vol. 15, Springer-Verlag: Eindhoven, The Netherlands, 2011, pp. 327–332. doi:10.1007/978-94-007-2482-2_52.

[23] N. S. Dhamankar, C. S. Martha, Y. Situ, K. M. Aikens, G. A. Blaisdell, A. S. Lyrintzis, Z. Li, Digital filter-based turbulent inflow generation for jet aeroacoustics on non-uniform structured grids, in: 52nd Aerospace Sciences Meeting, no. January, American Institute of Aeronautics and Astronautics, Reston, Virginia, USA, 2014, pp. 1–35. doi:10.2514/6.2014-1401.

[24] J. Allegrini, J. Carmeliet, Evaluation of the filtered noise turbulent inflow generation method, Flow, Turbulence and Combustion 98 (4) (2017) 1087–1115. doi:10.1007/s10494-016-9798-2.

[25] Y. Kim, I. P. Castro, Z. T. Xie, Divergence-free turbulence inflow conditions for large-eddy simulations with incompressible flow solvers, Computers and Fluids 84 (2013) 56–68. doi:10.1016/j.compfluid.2013.06.001.

[26] R. Ewert, The simulation of slat noise applying stochastic sound sources based on solenoidal digital filters (SDF), in: Euromech Colloquium 467: Turbulent Flow and Noise Generation July 18-20, 2005, American Institute of Aeronautics and Astronautics, Reston, Virigina, 2005. doi:10.2514/6.2005-2862.

[27] A. Smirnov, S. Shi, I. Celik, Random flow generation technique for large eddy simulations and particle-dynamics modeling, Journal of Fluids Engineering 123 (2) (2001) 359. doi:10.1115/1.1369598.

[28] J. Jimenez, Turbulent velocity fluctuations need not be Gaussian, Journal of Fluid Mechanics 376. doi:10.1017/S0022112098002432.

[29] R. D. Moser, J. Kim, N. N. Mansour, Direct numerical simulation of turbulent channel flow up to Reτ=590, Physics of Fluids 11 (4) (1999) 943–945. arXiv:1410.7809, doi:10.1063/1.869966.

[30] E. Touber, N. D. Sandham, Large-eddy simulation of low-frequency unsteadiness in a turbulent shock-induced separation bubble, Theoretical and Computational Fluid Dynamics 23 (2) (2009) 79–107. doi:10.1007/s00162-009-0103-z.

[31] S. Breuer, M. Schmidt, Extended synthetic turbulence inflow generator within a hybrid LES-URANS methodology for the prediction of non-equilibrium wall-bounded flows, Flow, Turbulence and Combustion 95 (4) (2015) 669–707. doi:10.1007/s10494-015-9639-8.

[32] K. Anupindi, R. D. Sandberg, Implementation and evaluation of an embedded LES-RANS solver, Flow, Turbulence and Combustion 98 (3) (2017) 697–724. doi:10.1007/s10494-016-9787-5.

[33] T. Okaze, A. Mochida, Cholesky decomposition-based generation of artificial inflow turbulence including scalar fluctuation, Computers and Fluids 159 (2017) 23–32. doi:10.1016/j.compfluid.2017.09.005.

[34] M. Ihme, Y. C. See, LES flamelet modeling of a three-stream MILD combustor: Analysis of flame sensitivity to scalar inflow conditions, Proceedings of the Combustion Institute 33 (1) (2011) 1309–1317. doi:10.1016/j.proci.2010.05.019.

[35] Y. Kim, Z. T. Xie, I. P. Castro, A forward stepwise method of inflow generation for LES, in: AIP Conference Proceedings, Vol. 1376, American Institute of Physics, 2011, pp. 134–136. doi:10.1063/1.3651856.

[36] S. Schmidt, M. Breuer, Source term based synthetic turbulence inflow generator for eddy-resolving predictions of an airfoil flow including a laminar separation bubble, Computers and Fluids 146 (2017) 1–22. doi:10.1016/j.compfluid.2016.12.023.

[37] I. Veloudis, Z. Yang, J. J. McGuirk, G. J. Page, A. Spencer, Novel implementation and assessment of a digital filter based approach for the generation of les inlet conditions, Flow, Turbulence and Combustion 79 (1) (2007) 1–24. doi:10.1007/s10494-006-9058-y.

[38] A. M. Kempf, S. Wysocki, M. Pettit, An efficient, parallel low-storage implementation of Klein's turbulence generator for LES and DNS, Computers and Fluids 60 (2012) 58–60. doi:10.1016/j.compfluid.2012.02.027.

[39] S. W. Smith, The scientist & engineer's guide To digital signal processing, California Technical Pub, 1999.

[40] G. I. Taylor, The spectrum of turbulence, Proceedings of the Royal Society A: Mathematical, Physical and Engineering Sciences 164 (919) (1938) 476–490. arXiv:arXiv:1205.0516v2, doi:10.1098/rspa.1938.0032.

[41] R. C. Booton, Nonlinear control systems with random inputs, IRE Transactions on Circuit Theory 1 (1) (1954) 9–18. doi:10.1109/TCT.1954.6373354.

[42] M. Grigoriu, Crossings of non Gaussian translation processes, Journal of Engineering Mechanics 110 (4) (1984) 610–620. doi:10.1061/(ASCE)0733-9399(1984)110:4(610).

[43] N. L. Johnson, Systems of frequency curves generated by methods of translation, Biometrika 36 (1-2) (1949) 149–176. doi:10.1093/biomet/36.1-2.149.

[44] K. R. Gurley, M. A. Tognarelli, A. Kareem, Analysis and simulation tools for wind engineering, Probabilistic Engineering Mechanics 12 (1) (1997) 9–31. doi:10.1016/S0266-8920(96)00010-0.

[45] F. Yamazaki, M. Shinozuka, Digital generation of non Gaussian stochastic fields, Journal of Engineering Mechanics 114 (7) (1988) 1183–1197. doi:10.1061/(ASCE)0733-9399(1988)114:7(1183).

[46] D. O. Smallwood, Generation of partially coherent stationary time histories with non-Gaussian distributions, in: Shock and vibration symposium, Monterey, CA, USA, 1996.
URL http://bit.ly/2bSgqbr

[47] K. O. Bowman, L. R. Shenton, Johnson's system of distributions, in: Encyclopedia of Statistical Sciences, Vol. 4, John Wiley & Sons, Inc., Hoboken, NJ, USA, 1982, pp. 303–314. doi:10.1002/0471667196.ess1309.pub2.

[48] H. J. H. Tuenter, An algorithm to determine the parameters of SU -curves in the Johnson system of probabillity distributions by moment matching, Journal of Statistical Computation and Simulation 70 (4) (2001) 325–347. doi:10.1080/00949650108812126.

[49] M. R. Flynn, On the moments of the 4-parameter lognormal distribution, Communications in Statistics - Theory and Methods 34 (4) (2005) 745–751. doi:10.1081/STA-200054397.

[50] O. OpenCFD, The open source CFD toolbox (2009).
URL http://www.openfoam.com/

[51] G. Comte-Bellot, S. Corrsin, Simple Eulerian time correlation of full-and narrow-band velocity signals in grid-generated, isotropic turbulence, Journal of Fluid Mechanics 48 (2) (1971) 273–337. doi:10.1017/S0022112071001599.

[52] S. Tavoularis, S. Corrsin, Experiments in nearly homogeneous turbulent shear flow with a uniform mean temperature gradient. Part 2. The fine structure, Journal of Fluid Mechanics 104 (1981) 349–367. doi:10.1017/S0022112081002942.

[53] P. Sagaut, Large eddy simulation for incompressible flows: An introduction, 3rd Edition, Scientific computation, Springer Berlin Heidelberg, 2006. doi:10.1007/b137536.
URL http://www.springer.com/us/book/9783540263449

[54] J. S. Baggett, J. Jimenez, A. G. Kravchenko, Resolution requirements in large-eddy simulation of shear flows, in: Annual Research Briefs - 1997, Stanford, CA, USA, 1997, pp. 51–66.

[55] R. I. Issa, Solution of the implicitly discretised fluid flow equations by operator-splitting, Journal of Computational Physics 62 (1) (1986) 40–65. arXiv:9809069v1, doi:10.1016/0021-9991(86)90099-9.

[56] NIST-SEMATECH, NIST/SEMATECH e-handbook of statistical methods, National Institute of Standards and Technology, 2003.
URL http://www.itl.nist.gov/div898/handbook/

[57] J. Jimenez, A. A. Wray, P. G. Saffman, R. S. Rogallo, The structure of intense vorticity in isotropic turbulence, Journal of Fluid Mechanics 255 (1993) 65–90. doi:10.1017/S0022112093002393.

[58] M. Farge, K. Schneider, CVS decomposition of 3D homogeneous turbulence using orthogonal wavelets, in: Center for Turbulence Research, 2000, pp. 305–317.

[59] D. Dietzel, D. Messig, F. Piscaglia, A. Montorfano, G. Olenik, O. T. Stein, A. Kronenburg, A. Onorati, C. Hasse, Evaluation of scale resolving turbulence generation methods for Large Eddy Simulation of turbulent flows, Computers and Fluids 93 (2014) 116–128. doi:10.1016/j.compfluid.2014.01.013.

[60] S. Tavoularis, S. Corrsin, Experiments in nearly homogenous turbulent shear flow with a uniform mean temperature gradient. Part 1, Journal of Fluid Mechanics 104 (EM6) (1981) 311–347. doi:10.1017/S0022112081002930.

[61] R. D. Moser, DNS data for turbulent channel flow (2007).
URL http://bit.ly/2rJeQ3u

[62] M. M. Fréchet, Sur quelques points du calcul fonctionnel, Rendiconti del Circolo Matematico di Palermo 22 (1) (1906) 1–72. doi:10.1007/BF03018603.

[63] T. Eiter, H. Mannila, Computing discrete Fréchet distance, Technical report, Technische Universität Wien, Wien (1994). doi:10.1.1.90.937.

[64] T. Eiter, H. Mannila, Distance measures for point sets and their computation, Acta Informatica 34 (2) (1997) 109–133. doi:10.1007/s002360050075.

[65] N. Michaud-Agrawal, E. J. Denning, T. B. Woolf, O. Beckstein, MDAnalysis: A toolkit for the analysis of molecular dynamics simulations, Journal of Computational Chemistry 32 (10) (2011) 2319–2327. arXiv:NIHMS150003, doi:10.1002/jcc.21787.

[66] R. J. Gowers, M. Linke, J. Barnoud, T. J. E. Reddy, M. N. Melo, S. L. Seyler, J. Domański, D. L. Dotson, S. Buchoux, I. M. Kenney, O. Beckstein, MDAnalysis: A Python package for the rapid analysis of molecular dynamics simulations, in: S. Benthall, S. Rostrup (Eds.), Proceedings of the 15th Python in Science Conference, 2016, pp. 98–105.

[67] S. L. Seyler, A. Kumar, M. F. Thorpe, O. Beckstein, Path similarity analysis: A method for quantifying macromolecular pathways, PLoS Computational Biology 11 (10). arXiv:1505.04807, doi:10.1371/journal.pcbi.1004568.

[68] D. B. Thomas, W. Luk, P. H. W. Leong, J. D. Villasenor, Gaussian random number generators, ACM Computing Surveys 39 (4). doi:10.1145/1287620.1287622.

[69] G. Marsaglia, W. W. Tsang, The Ziggurat method for generating random variables, Journal of the Geological Society of London 5 (8) (2000) 1–7. doi:10.18637/jss.v005.i08.

[70] D. Eddelbuettel, RcppZiggurat: 'Rcpp' integration of different "Ziggurat" normal RNG implementations (2015).

[71] P. H. W. Leong, G. Zhang, D.-U. Lee, W. Luk, J. D. Villasenor, A comment on the implementation of the Ziggurat method, Journal of Statistical Software 12 (7) (2005) 1–4. doi:10.1007/978-1-60327-198-1_26.

[72] J. F. Claerbout, Multidimensional recursive filters via a helix, Geophysics 63 (5) (1998) 1532–1541. doi:10.1190/1.1444449.

[73] E. W. Weisstein, Fourier transform–Gaussian.
URL http://mathworld.wolfram.com/FourierTransformGaussian.html

[74] E. W. Weisstein, Fourier transform–Exponential function.
URL http://mathworld.wolfram.com/FourierTransformExponentialFunction.html

[75] D. A. Dickey, W. A. Fuller, Distribution of the estimators for autoregressive time series with a unit root, Journal of the American Statistical Association 74 (366) (1979) 427. doi:10.2307/2286348.

[76] J. Grazzini, Analysis of the emergent properties: Stationarity and ergodicity, Jasss 15 (2). doi:10.18564/jasss.1929.

[77] D. Nicolaides, D. R. Honnery, J. Soria, Autocorrelation functions and the determination of integral length with reference to experimental and numerical data, in: 15th Australasian Fluid Mechanics Conference, Vol. 1, The University of Sydney, Sydney, Australia, 2004, pp. 1–4.

[78] P. D. Welch, The use of fast Fourier transform for the estimation of power spectra: A method based on time averaging over short, modified periodograms, IEEE Transactions on Audio and Electroacoustics 15 (2) (1967) 70–73. doi:10.1109/TAU.1967.1161901.

[79] P. J. Cameron, Colour schemes, Technical Note C, SRON Netherlands Institute for Space Research (1982). doi:10.1016/S0304-0208(08)73255-9.
URL http://bit.ly/2EtFBxl

[80] N. S. Neidell, Deterministic deconvolution operators - 3 point or 4 point?, Geophysics 37 (6) (1972) 1039–1042. doi:10.1190/1.1440312.

[81] J. F. Claerbout, M. Karrenbach, O. Balog, Earth soundings analysis: Processing versus inversion, 1992.

8. Figures and tables

Table 1: List of statistical measures used in the study.

	Measure	Tool for quantifications
i.	Statistical weak stationarity	Augmented Dickey-Fuller unit-root test [75].
ii.	Statistical weak ergodicity	Wald-Wolfowitz test [76].
iii.a.	Unbiased estimation of mean	$\widehat{\mu}_1 = \overline{x} = n^{-1} \sum_{i=1}^{n} x_i.$
iii.b.	Unbiased estimation of variance	$\widehat{\mu}_2 = (n-1)^{-1} \sum_{i=1}^{n} (x_i - \hat{\mu}_1)^2.$
iii.c.	Pearsonian coefficient of sample skewness	$\sqrt{\widehat{\beta}_1} = \frac{\hat{\mu}_3^2}{\hat{\mu}_2^3} = \frac{n^{-1} \sum_{i=1}^{n} (x_i - \hat{\mu}_1)^3}{\hat{\mu}_2^3}.$
iii.d.	Pearsonian coefficient of sample kurtosis	$\widehat{\beta}_2 = \frac{\hat{\mu}_4}{\hat{\mu}_2^2} = \frac{n^{-1} \sum_{i=1}^{n} (x_i - \hat{\mu}_1)^4}{\hat{\mu}_2^2}.$
iv.	One-point correlation tensor	$R_{xy} = z^{-1} \sum_{k=1}^{z} \left\{ \mathrm{T}^{-1} \sum_{i=\Delta_t}^{n\Delta_t} (x_{ki} - \hat{\mu}_{1_{x_k}})(y_{ki} - \hat{\mu}_{1_{y_k}}) \right\}.$
v.	Unbiased estimation of correlation functions	$\widehat{\rho}_{XY} = \frac{\hat{\mathrm{R}}_{XY}}{\hat{\mu}_{2_\mathrm{X}} \hat{\mu}_{2_\mathrm{Y}}}; \widehat{\mathrm{R}}_{XY} = (\mathrm{N}-a)^{-1} \sum_{i=\Delta_t}^{(\mathrm{N}-a)\Delta_t} x_i \, y_{i+a\Delta_t}.$
vi.	One-sided power spectral density function	Welch's method [78], window: Hanning, overlap: 50%.

n denotes the size of a discrete sample x, $\widehat{\cdot}$ the estimation operator, z the number of nodes along the statistically homogeneous direction, T the sample duration, Δ_t the time-step size, a the lag (time-offset) number, and N the maximum lag number.

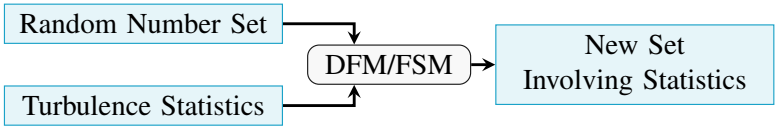

Figure 1: A diagram showing synthetic turbulence generation with DFM/FSM.[18]

[18] A color-blind proof and print-standard-friendly color scheme produced by [79] was used in this study.

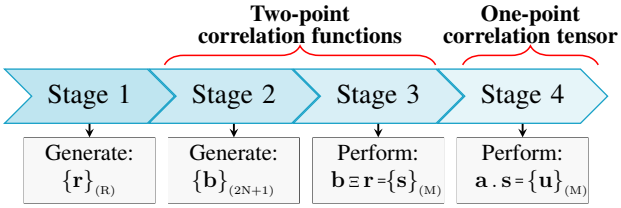

Figure 2: A general view of DFM/FSM model stages for a one-dimensional field of discrete points.

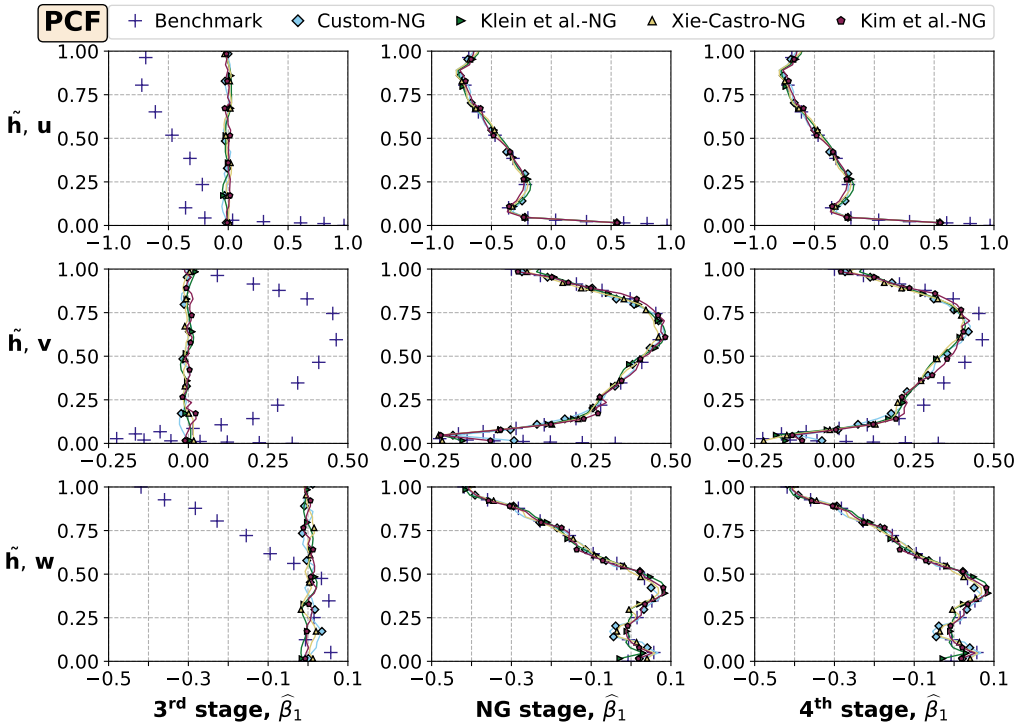

Figure 3: The Pearson's moment coefficient of sample skewness results, $\widehat{\beta}_1$, from DFM/FSM computations of the plane channel flow with smooth walls (PCF) [29]. From left to right, the 3$^{\text{rd}}$, non-Gaussian (NG) and 4$^{\text{th}}$ model stages and from top to bottom, velocity components, (u, v, w), are depicted. Of a subplot, the vertical axis denotes the normalized channel half-height, $\tilde{\text{h}}$=h/δ where h and δ are the half-height of the computational and benchmark domains, respectively. PCF is statistically symmetric along the channel centreline; hence, only the results belong to the half-height are shown. The horizontal axis stands for skewness, which was computed for each node-time-series and arithmetic averaged in the statistically homogeneous direction of the flow.

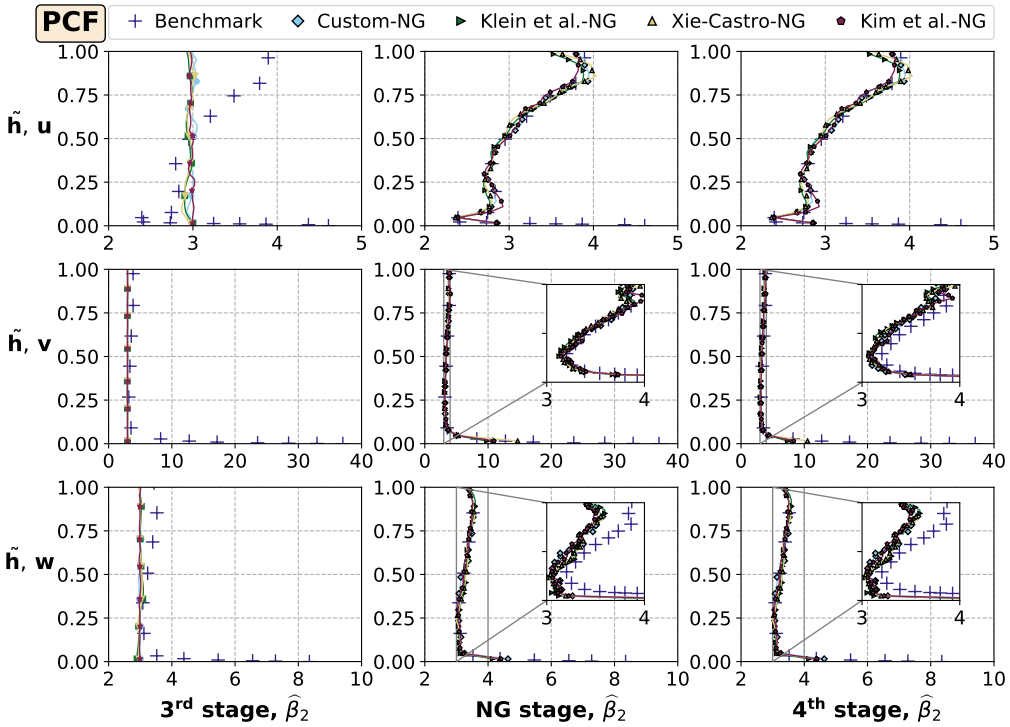

Figure 4: The Pearson's moment coefficient of sample kurtosis results, $\widehat{\beta}_2$, from DFM/FSM computations of the smooth-wall plane channel flow (PCF). The figure descriptions are as in Fig. 3.

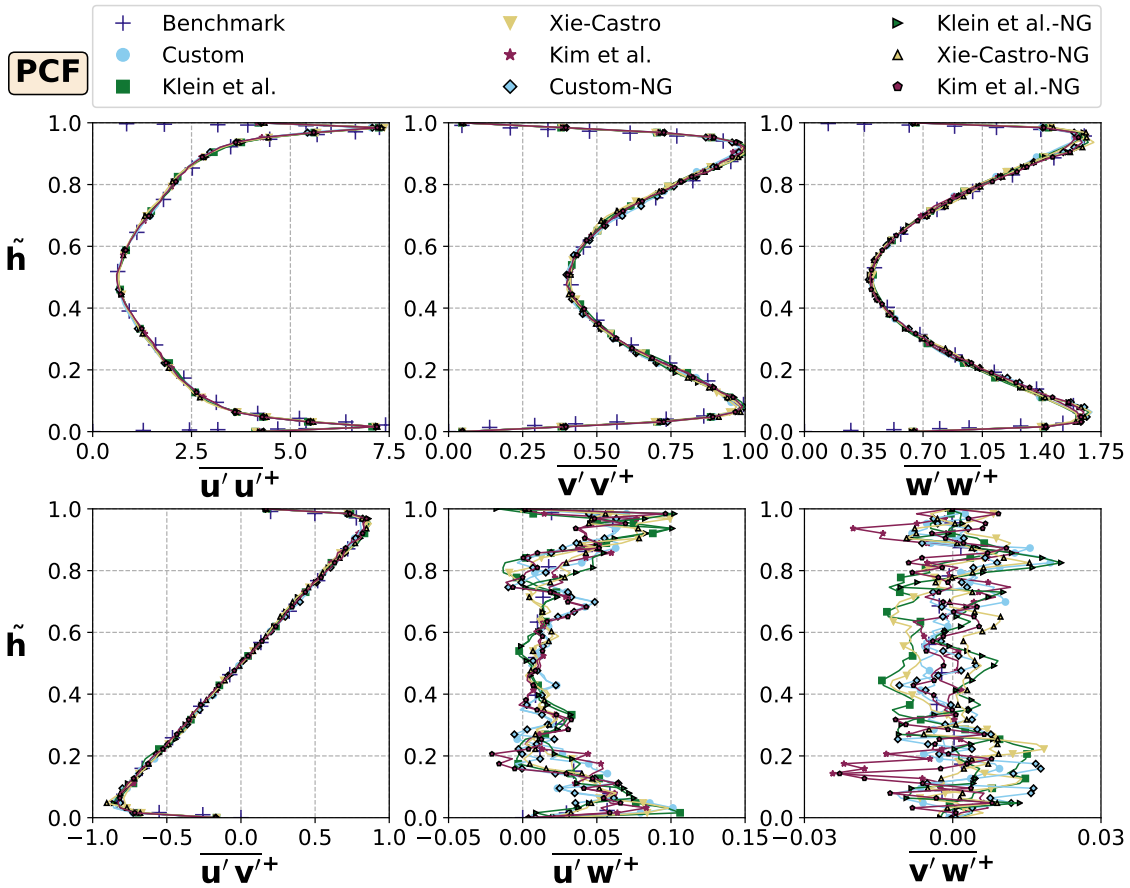

Figure 5: The results from DFM/FSM computations of the plane channel flow with smooth walls (PCF) [29] for one-spatial-point second-order correlation tensor of discrete fluctuating velocities, $\{u_i'(n\Delta, m\Delta_t)\, u_j'(n\Delta, m\Delta_t) \in \mathbb{Q}\}_{\{i,j,n,m\in\mathbb{N};\, i,j\in[1,3];\, n,m,\Delta_t>0\}}$. The vertical axis of a subplot stands for the normalized channel full-height, $\tilde{\text{h}}$=h/(2δ) where h and δ are the full-height of the computational domain and the half-height of the benchmark domain, respectively. The dependencies of the tensor components on space and time were reduced by arithmetic average in time and the statistically homogeneous direction of the flow; hence, $\overline{u_i'\, u_j'}^{+}$. $\{\text{-}\}$ denotes combined time and spanwise space average, and $\{\cdot\}^+$=$\{\cdot\}/u_\tau^2$ a normalization operator, where u_τ is the estimated friction velocity. The corresponding expression used in the computations is shown in Table 1.

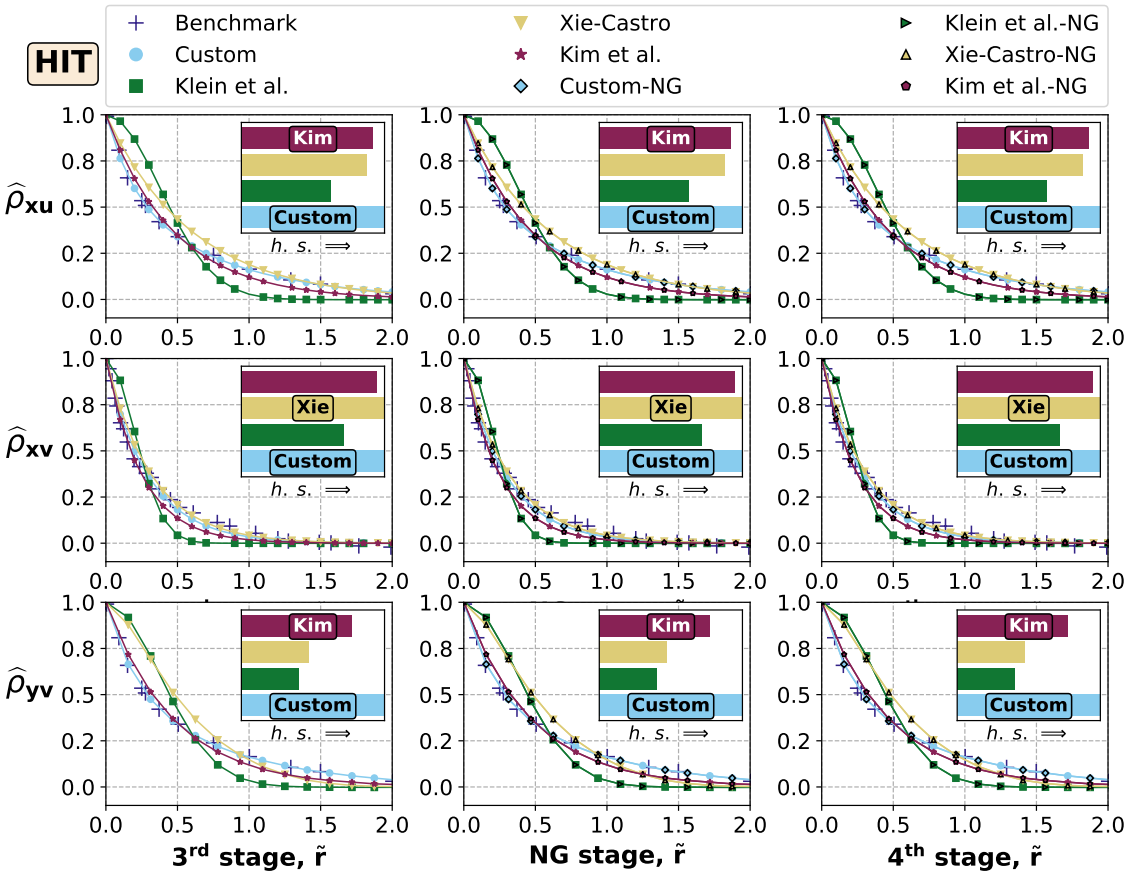

Figure 6: The two-spatial/temporal-point sample autocorrelation function results, $\widehat{\rho}_{mn}$, from the decaying homogeneous isotropic turbulence computations (HIT) [51]. In $\widehat{\rho}_{mn}$, 'm' stands for the measurement direction, and 'n' for the measured velocity component. $\widehat{\rho}_{mn}$s were computed for each node-time-series, and their arithmetic average was performed in the statistically homogeneous directions. From left to right, the 3$^{\text{rd}}$, non-Gaussian (NG) and 4$^{\text{th}}$ model stages are shown. From top to bottom, two longitudinal, $\widehat{\rho}_{xu}$ and $\widehat{\rho}_{yv}$, and one lateral, $\widehat{\rho}_{xv}$, autocorrelation functions are demonstrated. The horizontal axes denote the spatial lag, $\tilde{\mathbf{r}}$, normalized by the characteristic length M=0.0508 [m]. The horizontal bar chart illustrates the Fréchet distance of each model curve to the benchmark. Each bar is normalized by the most-similar-to-the-benchmark model curve. The maximum height of a bar is the unity, and '*h.s.*' with the arrow means the direction of *higher similarity*.

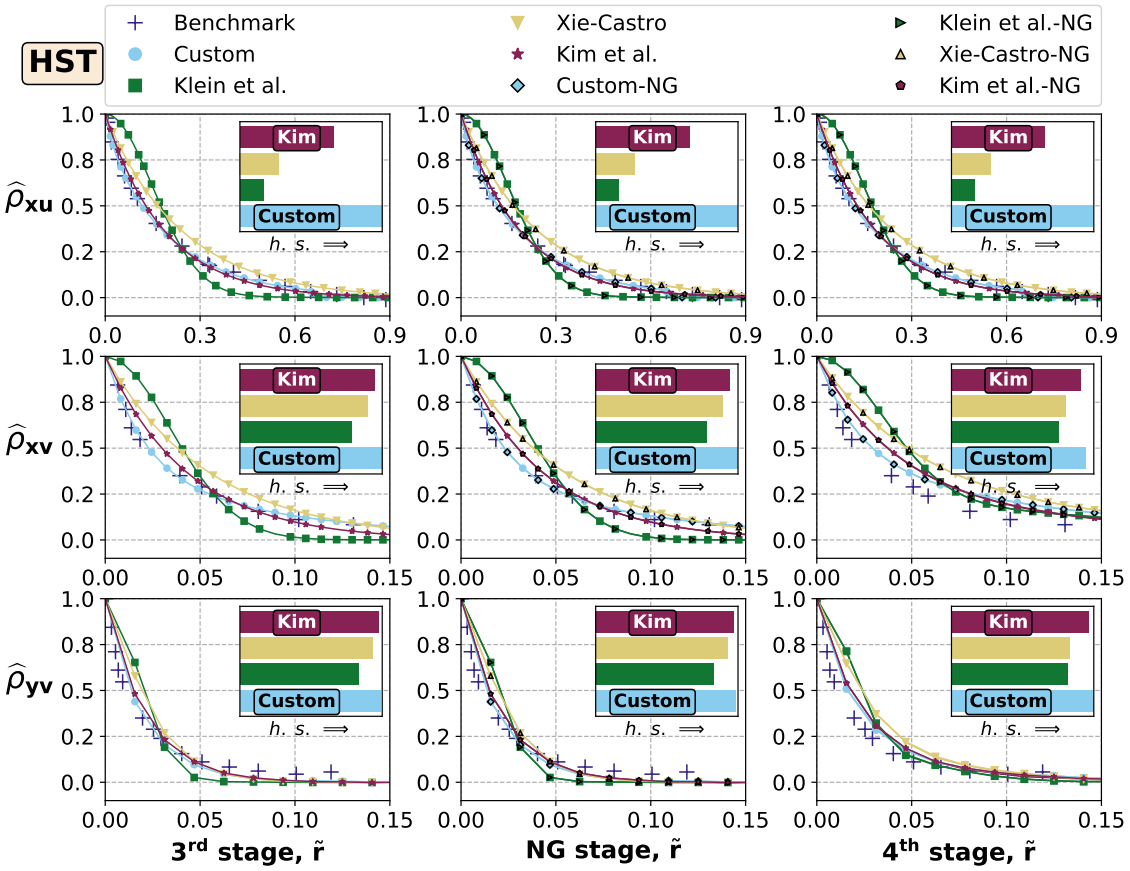

Figure 7: The two-spatial/temporal-point sample autocorrelation function results from the homogeneous shear turbulence computations (HST) [52]. The figure descriptions are the same with Fig. 6.

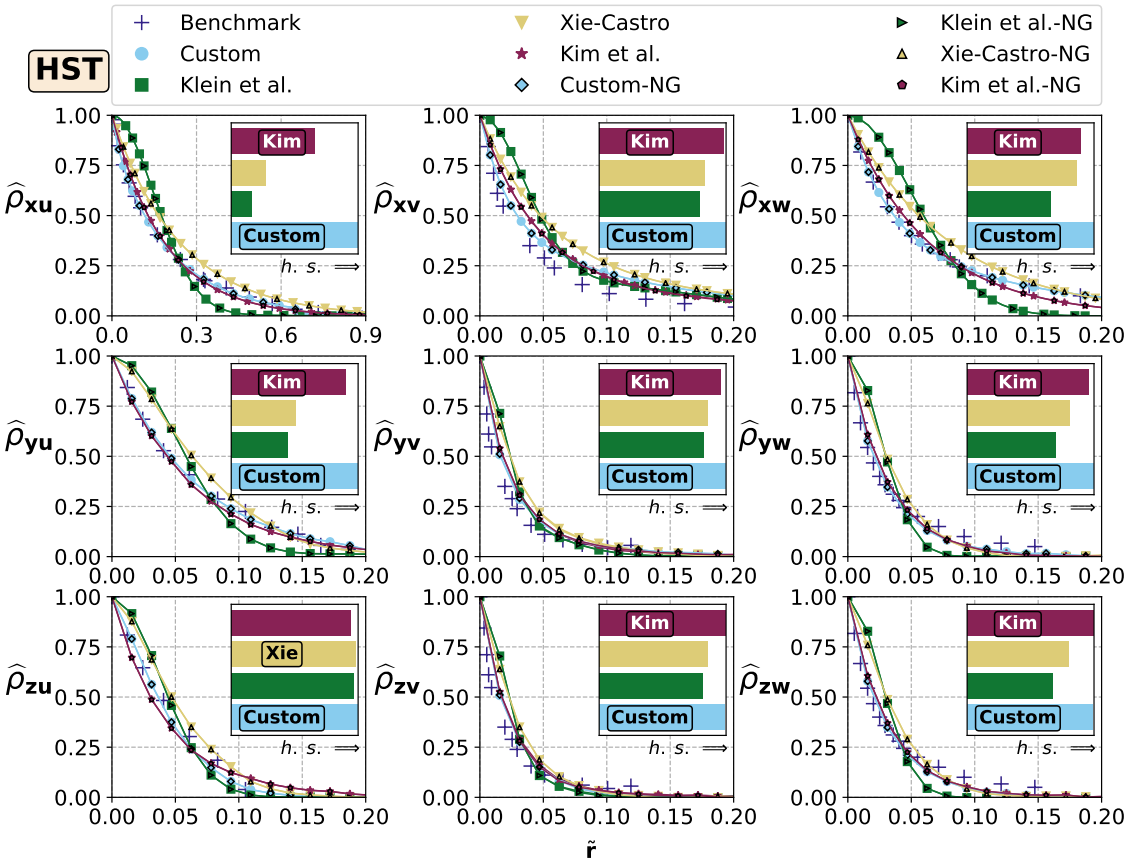

Figure 8: The two-spatial/temporal-point sample autocorrelation function results from the homogeneous shear turbulence computations (HST) [52]. Herein, all nine components of the correlation tensor are demonstrated. The figure descriptions are the same with Fig. 6.

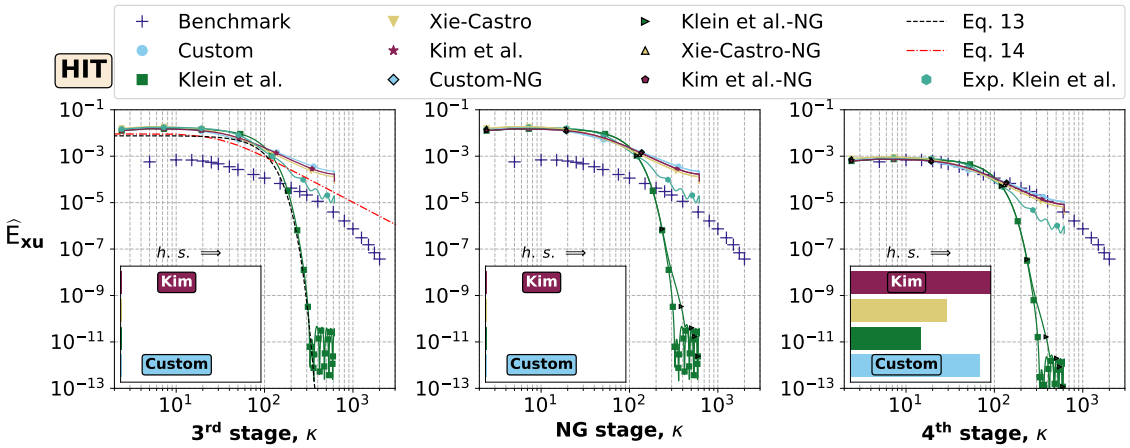

Figure 9: The sample one-dimensional power spectral density function results, $\widehat{E}_{\mathbf{xu}}$ [$m^3\,s^{-2}$], as a function of spatial wavenumber, κ [m^{-1}], from the decaying homogeneous isotropic turbulence computations (HIT) [51]. In $\widehat{E}_{\mathbf{xu}}$, '$\mathbf{x}$' stands for the measurement direction, and '$\mathbf{u}$' for the measured velocity component in this direction. 'Exp. Klein et al.' denotes Klein et al.'s method using the exponential-form filter function. $\widehat{E}_{\mathbf{xu}}$s were computed for time-series of each node, and their arithmetic average was performed in the statistically homogeneous directions. From left to right, the 3rd, non-Gaussian (NG) and 4th model stages are shown. The horizontal bar chart illustrates the Fréchet distance of each model curve to the benchmark. Each bar is normalized by the model curve which is the most similar to the benchmark. The maximum height of a bar is the unity, and '*h.s.*' with the arrow means the direction of *higher similarity*.

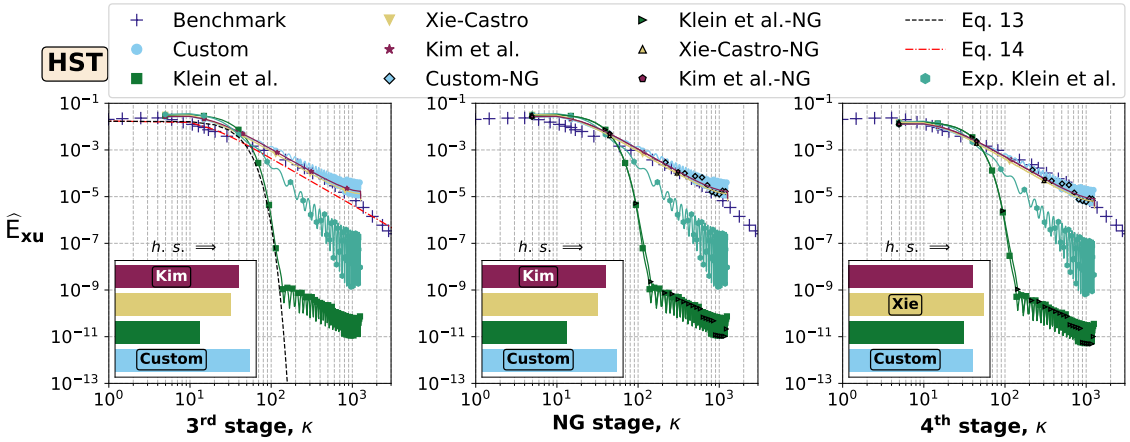

Figure 10: The sample one-dimensional power spectral density function results, $\widehat{E}_{\mathbf{xu}}$ [$m^3\,s^{-2}$], as a function of spatial wavenumber, κ [m^{-1}], from the homogeneous shear turbulence computations (HST) [52]. The figure descriptions are as in Fig. 9.

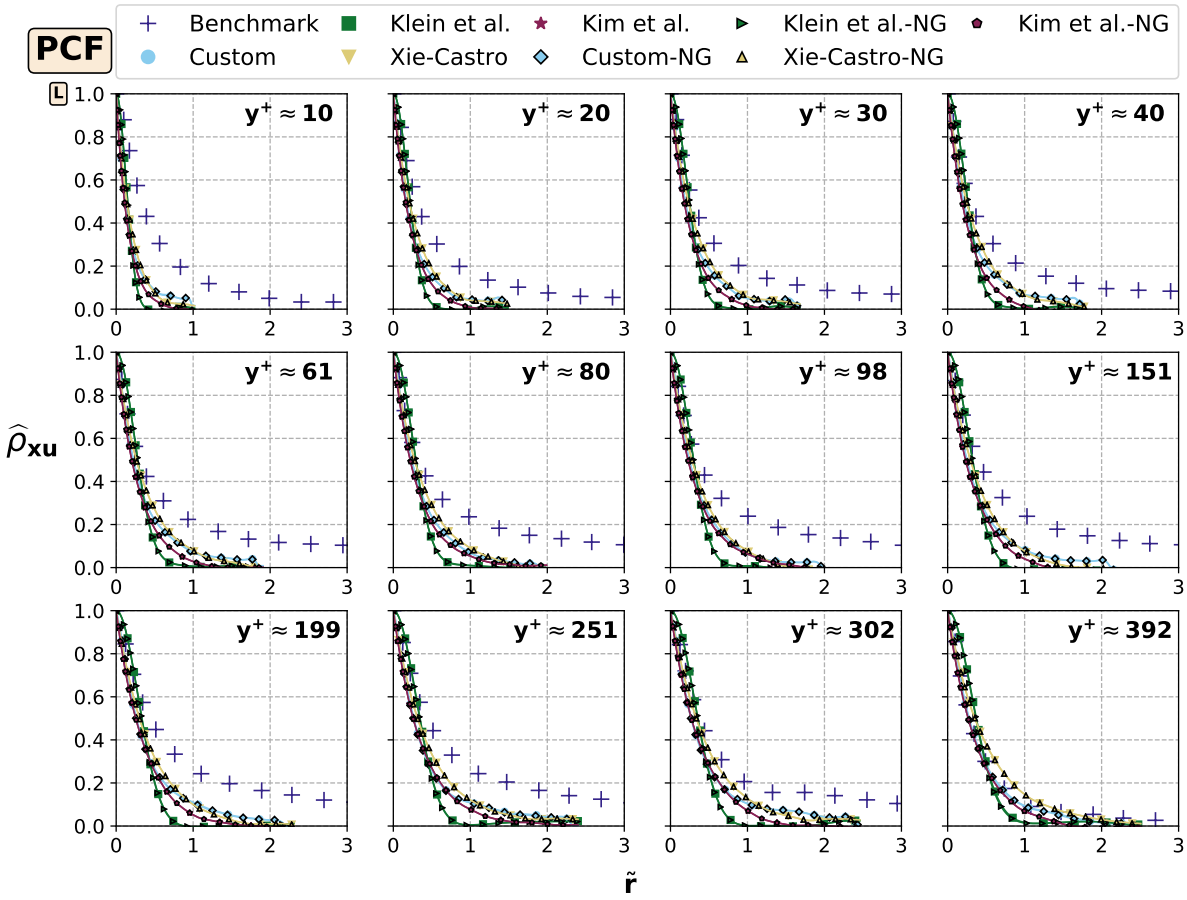

Figure 11: The two-spatial/temporal-point sample autocorrelation function results, $\widehat{\rho}_{xu}$, from the smooth-wall plane channel flow computations (PCF) [29] wherein a single set of correlation tensor, $\mathbf{L}$, was input. $\mathbf{y}^+$=$u_\tau\, y/\nu$ is the dimensionless wall distance, u_τ the friction velocity, ν the kinematic viscosity of the fluid, x the measurement direction, u the measured velocity component, and $\tilde{\mathbf{r}}$, the spatial lag normalized by the channel half-height, δ=1.0 [m]. The channel cross-section was segmented into 12 sections in the wall-normal direction, where the centre of a section is at the specified y^+. The same input correlation tensor was used for all sections. Only the channel half-height from the top wall is shown due to the statistical symmetry along the half-height. $\widehat{\rho}_{xu}$s were computed for each node-time-series, and their arithmetic average was performed in the statistically homogeneous spanwise direction and each section height.

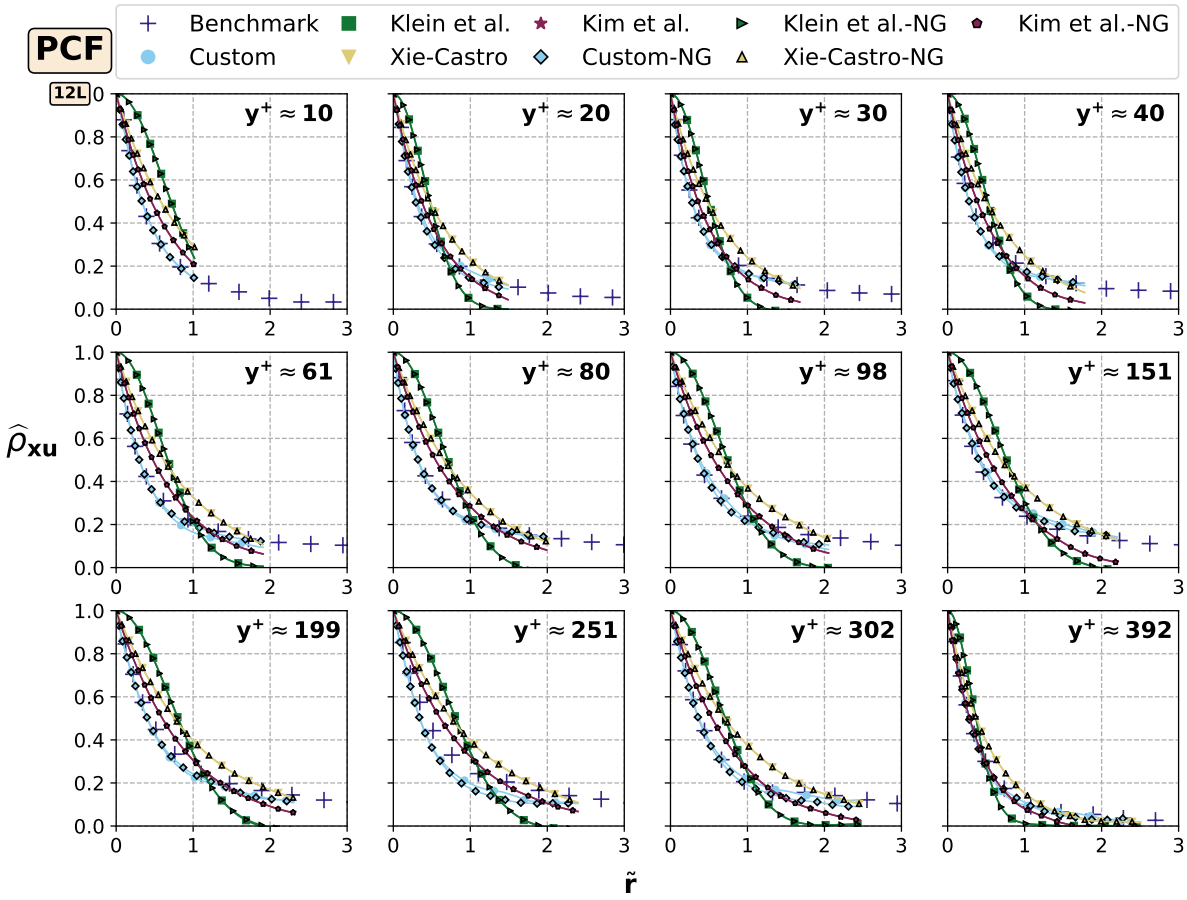

Figure 12: The two-spatial/temporal-point sample autocorrelation function results, $\widehat{\rho}_{xu}$, from the smooth-wall plane channel flow computations (PCF) [29] wherein twelve correlation tensors, **12L**, were input. The figure descriptions are the same with Fig. 11.

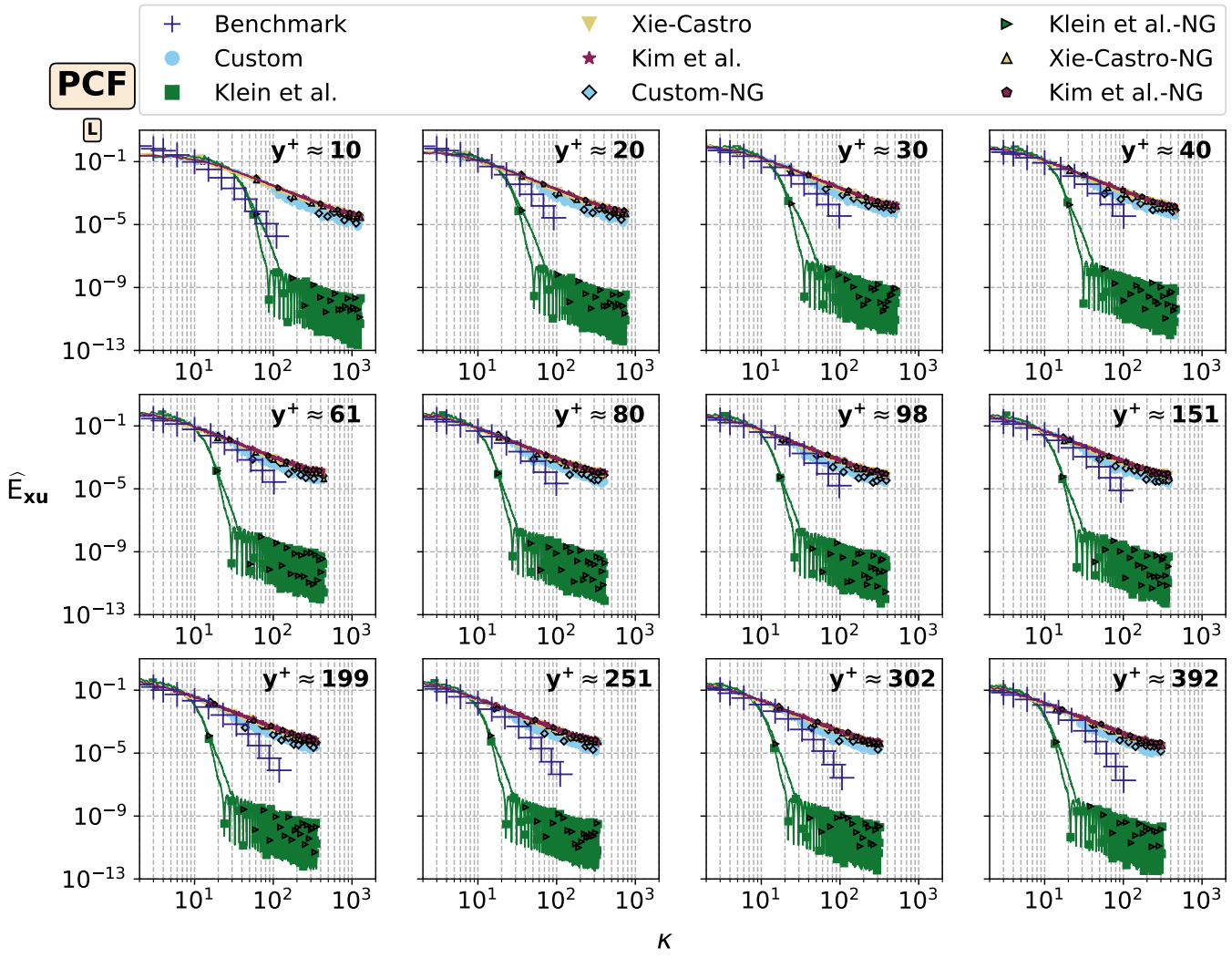

Figure 13: The sample one-dimensional one-sided power spectral density function results, $\widehat{\mathrm{E}}_{\mathbf{xu}}$ [$\mathrm{m}^3\,\mathrm{s}^{-2}$], as a function of spatial wavenumber, κ [m^{-1}], from the smooth-wall plane channel flow computations (PCF) [29]wherein a single set of correlation tensor, $\mathbf{L}$, was input. $\mathbf{y}^+$=$u_\tau\, y/\nu$ is the dimensionless wall distance, u_τ the friction velocity, ν the kinematic viscosity of the fluid, x the measurement direction, u the measured velocity component, and $\tilde{\mathbf{r}}$, the spatial lag normalized by the channel half-height, δ=1.0 [m]. The channel cross-section was segmented into 12 sections in the wall-normal direction, where the centre of a section is at the specified y^+. The same input correlation tensor was used for all sections. Only the channel half-height from the top wall is shown due to the statistical symmetry along the half-height. $\widehat{\rho}_{xu}$s were computed for each node-time-series, and their arithmetic average was performed in the statistically homogeneous spanwise direction and each section height.

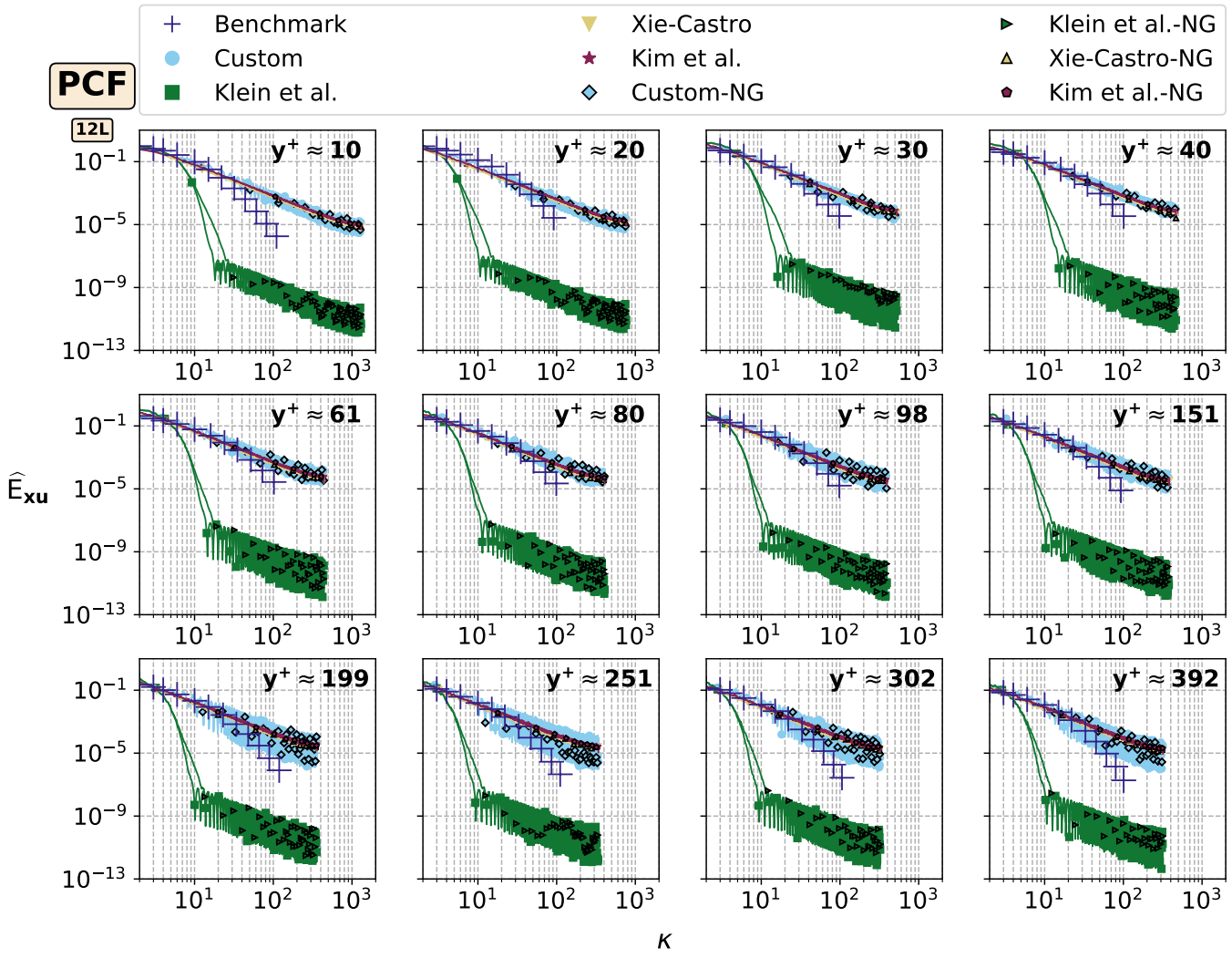

Figure 14: The sample one-dimensional one-sided power spectral density function results, $\widehat{\mathrm{E}}_{\mathbf{xu}}$ [$\mathrm{m}^3\,\mathrm{s}^{-2}$], as a function of spatial wavenumber, κ [m^{-1}], from the smooth-wall plane channel flow computations (PCF) [29] wherein twelve correlation tensors, **12L**, were input. The figure descriptions are as in Fig. 13.

Table 2: Approximate number of calls for the computational operations that are required by Eq. 10 and 11 during the transformation of a standard normal skewness-kurtosis pair to a target one. For brevity, operations needed for a single velocity component per time-step are shown.

Operations		S_U	S_L	S_B	Eq. 10 with arbitrary $F_{\text{IO}'_i}^{-1}$	Eq. 10 with Gaussian $F_{\text{IO}'_i}^{-1}$
Arithmetic Functions	Addition	-	-	1	2	1
	Subtraction	3	-	2	3	2
	Multiplication	-	-	-	3	5
	Division	3	-	3	1	1
Elementary Functions	$\exp(\cdot)$	2	1	1	-	-
Non-elementary Functions/Algorithms		-	-	-	1 $\text{erf}(\cdot)$ 1 Search algorithm	1 $\text{erf}(\cdot)$ 1 $\text{erf}^{-1}(\cdot)$

Table 3: The arithmetic average, $\overline{(\cdot)}$, and variance, $Var(\cdot)$, of the sample pairs from all nodes. A pair contains the sample mean, $\widehat{\mu}_1$, and sample standard deviation, $\sqrt{\widehat{\mu}_2}$, of a node-time-series. S-3, S-NG, and S-4 denote the 3rd, non-Gaussian, and 4th model stages, respectively. Each cell, $(\cdot|\cdot)$, represents values of $(\overline{(\cdot)}|Var(\cdot))$ rounded to two decimal places in the scientific notation.

	Custom			**Klein et al.**		
	S-3	S-NG	S-4	S-3	S-NG	S-4
$\widehat{\mu}_1$ (10^{-3}|10^{-4})	-1.19|3.88	-1.19|3.88	-0.26|0.18	0.16|3.53	0.16|3.53	0.04|0.161×10^{-2}
$\sqrt{\widehat{\mu}_2}$ (1|10^{-4})	1.00|0.94	1.00|0.86	0.22|0.04	1.00|1.25	1.00|1.14	0.22|0.06
	Xie-Castro			**Kim et al.**		
	S-3	S-NG	S-4	S-3	S-NG	S-4
$\widehat{\mu}_1$ (10^{-3}|10^{-4})	-0.61|4.58	-0.62|4.58	-0.14|0.22	0.95|5.43	0.95|5.43	0.21|0.26
$\sqrt{\widehat{\mu}_2}$ (1|10^{-4})	1.00|1.14	1.00|1.06	0.22|0.05	1.00|1.37	1.00|1.28	0.22|0.06

Table 4: The Pearson's moment coefficient of sample skewness, $\widehat{\beta}_1$, and sample kurtosis, $\widehat{\beta}_2$, obtained from Klein et a.'s method [13] computations of the decaying homogeneous isotropic turbulence (HIT) [51]. The other three methods produced results which were entirely in line with the table content. The benchmark skewness-kurtosis is ($\widehat{\beta}_1$-$\widehat{\beta}_2$)=(0.00-2.85) §4.1.2. S-3, S-NG, and S-4 denote the 3rd, non-Gaussian, and 4th model stages, respectively. Each cell value was computed as follows: first, sample skewness-kurtosis of each node-time-series were found, second the median of all values was calculated and then results were rounded to two decimal places.

			S-3	S-NG	S-4			S-3	S-NG	S-4
HIT	$\widehat{\beta}_1$ (10^{-3})	u	0.16	4.11	4.11	$\widehat{\beta}_2$	u	2.99	2.85	2.85
		v	-1.40	3.04	3.04		v	3.00	2.85	2.85
		w	0.49	4.85	4.85		w	3.00	2.85	2.85

Table 5: The Pearson's moment coefficient of sample skewness, $\widehat{\beta}_1$, and sample kurtosis, $\widehat{\beta}_2$, obtained from Klein et a.'s method [13] computations of the homogeneous shear turbulence (HST) [52]. The other three methods produced results which were entirely in line with the table content. The benchmark values can be found in §4.1.3. S-3, S-NG, and S-4 denote the 3rd, non-Gaussian, and 4th model stages, respectively. Each cell value was computed as follows: first, sample skewness-kurtosis of each node-time-series were found, second the median of all values was calculated and then results were rounded to two decimal places.

			S-3	S-NG	S-4			S-3	S-NG	S-4
		u	-4.75	-0.21×10^{3}	-0.21×10^{-3}		u	2.98	3.07	3.07
HST	$\widehat{\beta}_1$ (10^{-3})	v	1.34	0.16×10^{3}	0.13×10^{3}	$\widehat{\beta}_2$	v	2.99	3.19	3.12
		w	0.77	1.37	1.37		w	3.00	3.29	3.29

Appendix A. Appendix

Appendix A.1. Non-Gaussian random number set input-based approach

The method is a heuristic approach rather than a rigorous model. Withinside, the probability mass function (*pmf*) of generated random number sets is changed from the standard normal distribution to a prescribed non-Gaussian one. The basic assumption of the approach is that the *pmf* of the random number sets proportionately yields a similar *pmf* for the digital-filtered sets at the end of the filtering. Thus, such adjustment may suffice to designate the *pmf* of the outcome.

Appendix A.2. Deterministic deconvolution-based approach

In contrast to the first approach, the fundamental presumption of this approach is that the *pmf* of the first-stage random number sets is not similar to that of the last-stage digital-filtered sets; however, the former with a *particular pmf* may determine the *desired pmf* of the latter.

Recall that the basic mathematical operation in DFM is convolution (Eq. 2), which may be recast into a simplified form as: $\mathbf{s} = \mathbf{b} \star \mathbf{r}$, where $\star$ is the convolution operator. Herein, $\mathbf{b}$ and $\mathbf{r}$ are known sets; and, $\mathbf{s}$ is unknown.

Let $\mathbf{b}$ and $\mathbf{s}$ are known, and $\mathbf{r}$ is unknown in the same convolution relation. In principle, $\star$ may be reversed in order to obtain $\mathbf{r}$. This process is called *deconvolution*, which can be expressed as:

$$\mathbf{s} \boxed{*} \mathbf{b} = \mathbf{r}^* \approx \mathbf{r} \tag{A.1}$$

where $\boxed{*}$ is the deconvolution operator, and $\mathbf{r} = \mathbf{r}^* + \epsilon$ with ϵ an element-wise error field.

The second basic assumption is that the *particular pmf* of $\mathbf{r}$ may be found through the deconvolution: Consider a *desired pmf* $\mathbf{h}_{\mathbf{s}'}$, and let n random sets $\{\mathbf{s}'_m\}_{\{m\in[1,n]\,\&\,\mathbf{s}'_m\neq\mathbf{s}'_q \text{ if } m\neq q\}}$ are generated

according to $\mathbf{h}_{\mathbf{s}'}$. Then, $\mathbf{r}_m^* \approx \mathbf{r}_m$ may be computed through the deconvolution for known and constant $\mathbf{b}$. Denoting each *pmf* of $\{\mathbf{r}_m\}$ as h_i, a generic *pmf* for $\mathbf{r}$ might be approximated by the arithmetic average of h_i: i.e. $n^{-1}\sum_{i=1}^{n} h_i = \mathbf{h}_{\mathbf{r}}$ when $n \gg 1$. Finally, a new random number set $\mathbf{r}$ obeying the *pmf* of $\mathbf{h}_{\mathbf{r}}$ could be convolved with $\mathbf{b}$ to yield a digital-filtered random set $\mathbf{s}'$ which follows the desired $\mathbf{h}_{\mathbf{s}'}$.

In practice, arguably, no standard form of deconvolution exists, and its form depends upon various characteristics of its operands. Whilst $\mathbf{b}$ is always precisely known, the optimal choice for this study is the deterministic deconvolution ([80]), which may be defined as an arithmetic division of Fourier transformed operands in the frequency domain:

$$\mathbf{r} \approx \mathbf{r}^* = \mathscr{F}^{-1}\left\{\frac{\mathscr{F}\{\mathbf{s}\}}{\mathscr{F}\{\mathbf{b}\}}\right\} \tag{A.2}$$

where $\mathscr{F}\{\cdot\}$ the discrete fast Fourier transform operation, and $\mathscr{F}^{-1}\{\cdot\}$ its inverse.

Two challenges, however, exist in respect to the formulation. The first is that Eq. A.2 does not guarantee a definition of a solution due to the possibility of the presence of zero in the denominator term. The second challenge is the arithmetic division by a small number, which may cause spurious spikes in the output. [81, p. 86], therefore, proposed the following modification to Eq A.2 in order to alleviate the aforementioned challenges:

$$\mathbf{r} \approx \mathbf{r}^* = \mathscr{F}^{-1}\left\{\frac{\mathscr{F}\{\mathbf{s}\}\mathscr{F}\{\mathbf{b}\}^*}{\mathscr{F}\{\mathbf{b}\}\mathscr{F}\{\mathbf{b}\}^* + \epsilon^2}\right\} \tag{A.3}$$

where $\mathscr{F}\{\mathbf{b}\}^*$ is the complex conjugate of $\mathscr{F}\{\mathbf{b}\}$, and ϵ a small real number proportional to the arithmetic average of $\mathscr{F}\{\mathbf{b}\}\mathscr{F}\{\mathbf{b}\}^*$ such $\epsilon = \lambda\{\overline{\mathscr{F}\{\mathbf{b}\}\mathscr{F}\{\mathbf{b}\}^*}\}^2$ with a constant λ. For an illustrative example, [81, p. 87] set $\lambda = 0.03$; however, no range of values was particularly suggested.

Appendix A.3. PDF transformation-based approach

Appendix A.3.1. Derivations

The standard Gaussian CDF is:

$$\phi_{\mathrm{N}}(x) = \frac{1}{2} + \frac{1}{2}\,\mathrm{erf}\left(\frac{x}{\sqrt{2}}\right) \tag{A.4}$$

The standard Gaussian quantile function is:

$$\phi_{\mathrm{N}}^{-1}(x) = \sqrt{2}\,\mathrm{erf}^{-1}(2x-1) \tag{A.5}$$

S_U Unbounded family

The quantile function of Johnson S_U family:

$$F_{\mathrm{SU}}^{-1}(q;a,b) = \sinh\left[\frac{\phi^{-1}(q)-a}{b}\right] \tag{A.6}$$

The substitution of Eq. A.5 into Eq. A.6 yields the following:

$$\begin{aligned}
F_{\mathrm{SU}}^{-1}(q;a,b) &= \sinh\left[\frac{\sqrt{2}\,\mathrm{erf}^{-1}(2q-1)-a}{b}\right] \\
&= \sinh\left[\frac{\sqrt{2}\,\mathrm{erf}^{-1}\left[2\left(\frac{1}{2}+\frac{1}{2}\,\mathrm{erf}\left(\frac{x}{\sqrt{2}}\right)\right)-1\right]-a}{b}\right] \qquad q=\phi_{\mathrm{N}}(x) \quad \Rightarrow \\
&= \sinh\left[\frac{\sqrt{2}\,\mathrm{erf}^{-1}\left[\mathrm{erf}\left(\frac{x}{\sqrt{2}}\right)\right]-a}{b}\right] \qquad \mathrm{erf}^{-1}(\mathrm{erf}(x/\sqrt{2}))=x/\sqrt{2} \quad \Rightarrow \\
&= \sinh\left[\frac{x-a}{b}\right]
\end{aligned} \tag{A.7}$$

S_L Log-Normal family

The quantile function of Johnson S_L family:

$$F_{\mathrm{SL}}^{-1}(q;\sigma) = \exp\left[\sigma\phi^{-1}(q)\right] \tag{A.8}$$

The substitution of Eq. A.5 into Eq. A.8 yields the following:

$$F_{\mathrm{SL}}^{-1}(q;\sigma) = \exp\left[\sigma x\right] \tag{A.9}$$

S_B Bounded family

The quantile function of Johnson S_B family:

$$F_{\mathrm{SB}}^{-1}(q;a,b) = \frac{1}{1+\exp\left[\frac{-1}{b}\left\{\phi_{\mathrm{N}}^{-1}(q)-a\right\}\right]} \tag{A.10}$$

The substitution of Eq. A.5 into Eq. A.10 yields the following:

$$\begin{aligned}
F_{\mathrm{SB}}^{-1}(q;a,b) =& \frac{1}{1+\exp\left[\frac{-1}{b}\left\{\phi_{\mathrm{N}}^{-1}(q)-a\right\}\right]} \\
=& \frac{1}{1+\exp\left[\frac{-1}{b}\left\{\sqrt{2}\,\mathrm{erf}^{-1}(2q-1)-a\right\}\right]} \qquad q=\phi_{\mathrm{N}}(x) \quad \Rightarrow \\
=& \frac{1}{1+\exp\left[\frac{-1}{b}\left\{\sqrt{2}\,\mathrm{erf}^{-1}\left(2\left[\frac{1}{2}+\frac{1}{2}\,\mathrm{erf}\left(\frac{x}{\sqrt{2}}\right)\right]-1\right)-a\right\}\right]} \\
=& \frac{1}{1+\exp\left[\frac{-1}{b}\left\{\sqrt{2}\,\mathrm{erf}^{-1}\left(\mathrm{erf}\left(\frac{x}{\sqrt{2}}\right)\right)-a\right\}\right]} \qquad \mathrm{erf}^{-1}(\mathrm{erf}(x/\sqrt{2}))=x/\sqrt{2} \quad \Rightarrow \\
=& \frac{1}{1+\exp\left[\frac{a-x}{b}\right]}
\end{aligned} \tag{A.11}$$

Appendix A.3.2. S_U Unbounded family [48]

$$\beta_1 = \left(\omega+1-\sqrt{4+2\left[\omega^2-\frac{\beta_2+3}{\omega^2+2\omega+3}\right]}\right)\left(\omega+1+\frac{1}{2}\sqrt{4+2\left[\omega^2-\frac{\beta_2+3}{\omega^2+2\omega+3}\right]}\right)^2 \tag{A.12}$$

$$m = -2+\sqrt{4+2\left[\omega^2-\frac{\beta_2+3}{\omega^2+2\omega+3}\right]} \tag{A.13}$$

$$\mu_U = \mathrm{sign}(\beta_1^2)\sqrt{\frac{\omega+1}{2}\left(\frac{\omega-1}{m}-1\right)} \tag{A.14}$$

$$\sigma_U = (\omega-1)\sqrt{\frac{\omega+1}{2m}} \tag{A.15}$$

$$\delta = \frac{1}{\sqrt{\log(\omega)}} \tag{A.16}$$

$$\gamma = \frac{-\text{sign}(\beta_1^2)\sinh^{-1}\left(\sqrt{\frac{\omega+1}{2\omega}\left(\frac{\omega-1}{m}-1\right)}\right)}{\sqrt{\ln\omega}} \tag{A.17}$$

Appendix A.3.3. S_B Bounded family

$$\beta_1^2 = \left(\frac{2\mu^3 - 3\mu\mu_2 + \mu_3}{\sigma^3}\right)^2 \tag{A.18}$$

$$\beta_2 = \frac{-3\mu^4 + 6\mu^2\mu_2 - 4\mu\mu_3 + \mu_4}{\sigma^4} \tag{A.19}$$

$$\mu = \frac{\text{A} - \text{B}}{\text{CD}} \tag{A.20}$$

$$\mu_2 = \mu(1-\delta\gamma) + \frac{\delta}{\text{CD}}\left(\text{A}_\gamma - \text{B}_\gamma - \mu\text{C}_\gamma\text{D}\right) \tag{A.21}$$

$$\mu_3 = \mu + 1.5\delta\mu_\gamma + 0.5\delta^2\mu_{\gamma^2} \tag{A.22}$$

$$\mu_4 = \mu + \frac{11}{6}\delta\mu_\gamma + \delta^2\mu_{\gamma^2} + \frac{1}{6}\delta^3\mu_{\gamma^3} \tag{A.23}$$

$$\text{A} = \frac{1}{2\delta} + \frac{1}{\delta}\sum_{n=1}^{\infty}\left\{\exp\left(\frac{-n^2}{2\delta^2}\right)\cosh\left(\frac{n(1-2\delta\gamma)}{2\delta^2}\right)\text{sech}\left(\frac{n}{2\delta^2}\right)\right\} \tag{A.24}$$

$$\text{A}_\gamma = -\frac{1}{\delta^2}\sum_{n=1}^{\infty}\left\{n\exp\left(\frac{-n^2}{2\delta^2}\right)\sinh\left(\frac{n(1-2\delta\gamma)}{2\delta^2}\right)\text{sech}\left(\frac{n}{2\delta^2}\right)\right\} \tag{A.25}$$

$$\text{A}_{\gamma^2} = \frac{1}{\delta^3}\sum_{n=1}^{\infty}\left\{n^2\exp\left(\frac{-n^2}{2\delta^2}\right)\cosh\left(\frac{n(1-2\delta\gamma)}{2\delta^2}\right)\text{sech}\left(\frac{n}{2\delta^2}\right)\right\} \tag{A.26}$$

$$\mathrm{A}_{\gamma^3} = -\frac{1}{\delta^4}\sum_{n=1}^{\infty}\left\{n^3\exp\left(\frac{-n^2}{2\delta^2}\right)\sinh\left(\frac{n(1-2\delta\gamma)}{2\delta^2}\right)\operatorname{sech}\left(\frac{n}{2\delta^2}\right)\right\} \tag{A.27}$$

$$\mathrm{B} = 2\pi\delta\sum_{n=1}^{\infty}\left\{\exp\left(-\frac{1}{2}(2n-1)^2\pi^2\delta^2\right)\sin\left((2n-1)\pi\delta\gamma\right)\operatorname{cosech}\left((2n-1)\pi^2\delta^2\right)\right\} \tag{A.28}$$

$$\mathrm{B}_{\gamma} = 2(\pi\delta)^2\sum_{n=1}^{\infty}\left\{(2n\text{-}1)\exp\left(-\frac{1}{2}(2n\text{-}1)^2\pi^2\delta^2\right)\cos\left((2n\text{-}1)\pi\delta\gamma\right)\operatorname{cosech}\left((2n\text{-}1)\pi^2\delta^2\right)\right\} \tag{A.29}$$

$$\mathrm{B}_{\gamma^2} = -2(\pi\delta)^3\sum_{n=1}^{\infty}\left\{-(2n\text{-}1)^2\exp\left(-\frac{1}{2}(2n\text{-}1)^2\pi^2\delta^2\right)\sin\left((2n\text{-}1)\pi\delta\gamma\right)\operatorname{cosech}\left((2n\text{-}1)\pi^2\delta^2\right)\right\} \tag{A.30}$$

$$\mathrm{B}_{\gamma^3} = -2(\pi\delta)^4\sum_{n=1}^{\infty}\left\{-(2n\text{-}1)^3\exp\left(-\frac{1}{2}(2n\text{-}1)^2\pi^2\delta^2\right)\cos\left((2n\text{-}1)\pi\delta\gamma\right)\operatorname{cosech}\left((2n\text{-}1)\pi^2\delta^2\right)\right\} \tag{A.31}$$

$$\mathrm{C} = 1 + 2\sum_{n=1}^{\infty}\left\{\exp\left(-2n^2\pi^2\delta^2\right)\cos\left(2n\pi\delta\gamma\right)\right\} \tag{A.32}$$

$$\mathrm{C}_{\gamma} = -4\pi\delta\sum_{n=1}^{\infty}\left\{n\exp\left(-2n^2\pi^2\delta^2\right)\sin\left(2n\pi\delta\gamma\right)\right\} \tag{A.33}$$

$$\mathrm{C}_{\gamma^2} = -8(\pi\delta)^2\sum_{n=1}^{\infty}\left\{n^2\exp\left(-2n^2\pi^2\delta^2\right)\cos\left(2n\pi\delta\gamma\right)\right\} \tag{A.34}$$

$$\mathrm{C}_{\gamma^3} = 16(\pi\delta)^3\sum_{n=1}^{\infty}\left\{n^3\exp\left(-2n^2\pi^2\delta^2\right)\sin\left(2n\pi\delta\gamma\right)\right\} \tag{A.35}$$

$$\mathrm{D} = \sqrt{2\pi}\exp\left(\frac{\gamma^2}{2}\right) \tag{A.36}$$

$$\mathrm{D}_{\gamma} = \gamma \mathrm{D} \tag{A.37}$$

$$\mathrm{D}_{\gamma^2} = (\gamma^2 + 1)\mathrm{D} \tag{A.38}$$

$$\mathrm{D}_{\gamma^3} = (\gamma^3 + 3\gamma)\mathrm{D} \tag{A.39}$$

$$\mu_{\gamma} = \frac{\mathrm{A}_{\gamma}}{\mathrm{CD}} - \frac{\mathrm{ADC}_{\gamma}}{(\mathrm{CD})^2} - \frac{\mathrm{ACD}_{\gamma}}{(\mathrm{CD})^2} - \left(\frac{\mathrm{B}_{\gamma}}{\mathrm{CD}} - \frac{\mathrm{BDC}_{\gamma}}{(\mathrm{CD})^2} - \frac{\mathrm{BCD}_{\gamma}}{(\mathrm{CD})^2} \right) \tag{A.40}$$

$$\begin{aligned}
\mu_{\gamma^2} = & \frac{\mathrm{A}_{\gamma}}{\mathrm{CD}} - \frac{\mathrm{A}_{\gamma}\mathrm{C}_{\gamma}}{\mathrm{C}^2\mathrm{D}} - \frac{\mathrm{A}_{\gamma}\mathrm{D}_{\gamma}}{\mathrm{CD}^2} \\
& - \frac{\mathrm{A}_{\gamma}\mathrm{C}_{\gamma}}{\mathrm{C}^2\mathrm{D}} - \frac{\text{-}2\mathrm{AC}_{\gamma}^2}{\mathrm{C}^3\mathrm{D}} - \frac{\text{-}\mathrm{AC}_{\gamma}\mathrm{D}_{\gamma}}{\mathrm{C}^2\mathrm{D}^2} - \frac{\mathrm{AC}_{\gamma^2}}{\mathrm{C}^2\mathrm{D}} \\
& - \frac{\mathrm{A}_{\gamma}\mathrm{D}_{\gamma}}{\mathrm{CD}^2} - \frac{\text{-}\mathrm{AC}_{\gamma}\mathrm{D}_{\gamma}}{\mathrm{C}^2\mathrm{D}^2} - \frac{\text{-}2\mathrm{AD}_{\gamma}^2}{\mathrm{CD}^3} - \frac{\mathrm{AD}_{\gamma^2}}{\mathrm{CD}^2} \\
& - \frac{\mathrm{B}_{\gamma}}{\mathrm{CD}} + \frac{\mathrm{B}_{\gamma}\mathrm{C}_{\gamma}}{\mathrm{C}^2\mathrm{D}} + \frac{\mathrm{B}_{\gamma}\mathrm{D}_{\gamma}}{\mathrm{CD}^2} \\
& + \frac{\mathrm{B}_{\gamma}\mathrm{C}_{\gamma}}{\mathrm{C}^2\mathrm{D}} + \frac{\text{-}2\mathrm{BC}_{\gamma}^2}{\mathrm{C}^3\mathrm{D}} + \frac{\text{-}\mathrm{BC}_{\gamma}\mathrm{D}_{\gamma}}{\mathrm{C}^2\mathrm{D}^2} + \frac{\mathrm{BC}_{\gamma^2}}{\mathrm{C}^2\mathrm{D}} \\
& + \frac{\mathrm{B}_{\gamma}\mathrm{D}_{\gamma}}{\mathrm{CD}^2} + \frac{\text{-}\mathrm{BC}_{\gamma}\mathrm{D}_{\gamma}}{\mathrm{C}^2\mathrm{D}^2} + \frac{\text{-}2\mathrm{BD}_{\gamma}^2}{\mathrm{CD}^3} + \frac{\mathrm{BD}_{\gamma^2}}{\mathrm{CD}^2}
\end{aligned} \tag{A.41}$$

$$
\begin{aligned}
\mu_{\gamma^3}(\mathrm{x}) =& \frac{-\mathrm{x}_{\gamma^2}\mathrm{C}_\gamma}{\mathrm{C}^2\mathrm{D}} + \frac{-\mathrm{x}_{\gamma^2}\mathrm{D}_\gamma}{\mathrm{C}\mathrm{D}^2} + \frac{\mathrm{x}_{\gamma^3}}{\mathrm{C}\mathrm{D}} \\
& - \frac{-2\mathrm{x}_\gamma(\mathrm{C}_\gamma)^2}{\mathrm{C}^3\mathrm{D}} - \frac{-\mathrm{x}_\gamma\mathrm{C}_\gamma\mathrm{D}_\gamma}{\mathrm{C}^2\mathrm{D}^2} - \frac{\mathrm{x}_{\gamma^2}\mathrm{C}_\gamma}{\mathrm{C}^2\mathrm{D}} - \frac{\mathrm{x}_\gamma\mathrm{C}_{\gamma^2}}{\mathrm{C}^2\mathrm{D}} \\
& - \frac{-\mathrm{x}_\gamma\mathrm{C}_\gamma\mathrm{D}_\gamma}{\mathrm{C}^2\mathrm{D}^2} - \frac{-2\mathrm{x}_\gamma(\mathrm{D}_\gamma)^2}{\mathrm{C}\mathrm{D}^3} - \frac{(\mathrm{x}_\gamma)^2\mathrm{D}}{\mathrm{C}\mathrm{D}^2} - \frac{\mathrm{x}(\mathrm{D}_\gamma)^2}{\mathrm{C}\mathrm{D}^2} \\
& - \frac{-2\mathrm{x}_\gamma(\mathrm{C}_\gamma)^2}{\mathrm{C}^3\mathrm{D}} - \frac{-\mathrm{x}_\gamma\mathrm{C}_\gamma\mathrm{D}_\gamma}{\mathrm{C}^2\mathrm{D}^2} - \frac{\mathrm{x}_{\gamma^2}\mathrm{C}_\gamma}{\mathrm{C}^2\mathrm{D}} - \frac{\mathrm{x}_\gamma\mathrm{C}_{\gamma^2}}{\mathrm{C}^2\mathrm{D}} \\
& - \frac{-2\mathrm{x}_\gamma(\mathrm{C}_\gamma)^2}{\mathrm{C}^3\mathrm{D}} - \frac{2(\mathrm{C}_\gamma)^2\mathrm{D}_\gamma}{\mathrm{D}^2\mathrm{C}^3} - \frac{6\mathrm{x}(\mathrm{C}_\gamma)^3}{\mathrm{C}^4\mathrm{D}} - \frac{-4\mathrm{x}\mathrm{C}_\gamma\mathrm{C}_{\gamma^2}}{\mathrm{C}^3\mathrm{D}} \\
& - \frac{-\mathrm{x}_\gamma\mathrm{C}_\gamma\mathrm{D}_\gamma}{\mathrm{C}^2\mathrm{D}^2} - \frac{2(\mathrm{C}_\gamma)^2\mathrm{D}_\gamma}{\mathrm{C}^3\mathrm{D}^2} - \frac{2\mathrm{C}_\gamma(\mathrm{D}_\gamma)^2}{\mathrm{C}^2\mathrm{D}^3} - \frac{-\mathrm{x}\mathrm{D}_{\gamma^2}\mathrm{C}_\gamma}{\mathrm{C}^2\mathrm{D}^2} - \frac{-\mathrm{x}\mathrm{C}_{\gamma^2}\mathrm{D}_\gamma}{\mathrm{C}^2\mathrm{D}^2} \\
& - \frac{\mathrm{x}_\gamma\mathrm{C}_{\gamma^2}}{\mathrm{C}^2\mathrm{D}} - \frac{-2\mathrm{x}\mathrm{C}_\gamma\mathrm{C}_{\gamma^2}}{\mathrm{C}^3\mathrm{D}} - \frac{-\mathrm{x}\mathrm{C}_{\gamma^2}\mathrm{D}_\gamma}{\mathrm{C}^2\mathrm{D}^2} - \frac{\mathrm{x}\mathrm{C}_{\gamma^3}}{\mathrm{C}^2\mathrm{D}} \\
& - \frac{-\mathrm{x}_\gamma\mathrm{C}_\gamma\mathrm{D}_\gamma}{\mathrm{C}^2\mathrm{D}^2} - \frac{-2\mathrm{x}_\gamma(\mathrm{D}_\gamma)^2}{\mathrm{C}\mathrm{D}^3} - \frac{\mathrm{x}_{\gamma^2}\mathrm{D}_\gamma}{\mathrm{C}\mathrm{D}^2} - \frac{\mathrm{x}_\gamma\mathrm{D}_{\gamma^2}}{\mathrm{C}\mathrm{D}^2} \\
& - \frac{-\mathrm{x}_\gamma\mathrm{C}_\gamma\mathrm{D}_\gamma}{\mathrm{C}^2\mathrm{D}^2} - \frac{2\mathrm{x}(\mathrm{D}_\gamma)^2\mathrm{C}_\gamma}{\mathrm{C}^2\mathrm{D}^3} - \frac{-\mathrm{x}\mathrm{C}_\gamma\mathrm{D}_{\gamma^2}}{\mathrm{C}^2\mathrm{D}^2} - \frac{2\mathrm{x}(\mathrm{C}_\gamma)^2\mathrm{D}_\gamma}{\mathrm{C}^3\mathrm{D}^2} - \frac{-\mathrm{x}\mathrm{C}_{\gamma^2}\mathrm{D}_\gamma}{\mathrm{C}^2\mathrm{D}^2} \\
& - \frac{-2\mathrm{x}_\gamma(\mathrm{D}_\gamma)^2}{\mathrm{C}\mathrm{D}^3} - \frac{2\mathrm{x}\mathrm{C}_\gamma(\mathrm{D}_\gamma)^2}{\mathrm{C}^2\mathrm{D}^3} - \frac{-4\mathrm{x}\mathrm{D}_\gamma\mathrm{D}_{\gamma^2}}{\mathrm{C}\mathrm{D}^3} - \frac{6\mathrm{x}(\mathrm{D}_\gamma)^3}{\mathrm{C}\mathrm{D}^4} \\
& - \frac{\mathrm{x}_\gamma\mathrm{D}_{\gamma^2}}{\mathrm{C}\mathrm{D}^2} - \frac{-\mathrm{x}\mathrm{C}_\gamma\mathrm{D}_{\gamma^2}}{\mathrm{C}^2\mathrm{D}^2} - \frac{-2\mathrm{x}\mathrm{D}_\gamma\mathrm{D}_{\gamma^2}}{\mathrm{C}\mathrm{D}^3} - \frac{\mathrm{x}\mathrm{D}_{\gamma^3}}{\mathrm{C}\mathrm{D}^2}
\end{aligned}
\tag{A.42}
$$

$$
\mu_{\gamma^3} = \mu_{\gamma^3}(\mathrm{A}) + \mu_{\gamma^3}(\mathrm{B}) \tag{A.43}
$$

$$
\mu_B = \mu \tag{A.44}
$$

$$
\sigma_B = \mathrm{sign}(\beta_1)\sqrt{\mu_2 - \mu^2} \tag{A.45}
$$

Appendix A.3.4. Criterion

$$
g(\beta_2) = (\omega_1 - 1)(\omega_2 + 2)^2 \sim \beta_1 \tag{A.46}
$$

$$
\omega_1 = \frac{1}{2}\left(-1 + \sqrt{d} + \sqrt{\frac{4}{\sqrt{d}} - d - 3}\right) \tag{A.47}
$$

$$\omega_2 = \sqrt{\text{-}1 + \sqrt{2(\beta_2 - 1)}} \tag{A.48}$$

$$d = \text{-}1 + \sqrt[3]{7 + 2\beta_2 + 2\sqrt{D}} - \sqrt[3]{2\sqrt{D} - 7 - 2\beta_2} \tag{A.49}$$

$$D = \frac{(3 + \beta_2)(16\beta_2^2 + 87\beta_2 + 171)}{27} \tag{A.50}$$

Appendix A.4. Discrete Fréchet distance metric [63, p. 2]

Let $\{\mathbf{P}_{\Delta_t}\}_{\{0\leq\Delta_t\leq \mathrm{T};\, 1\leq t\leq p;\, t\in\mathbb{Z}^+\}}$=$\{P_{\Delta_1}, \ldots, P_{\Delta_p}\}$, and similarly $\{\mathbf{Q}_{\Delta_t}\}$=$\{Q_{\Delta_1}, \ldots, Q_{\Delta_q}\}$, be two the-same-size discrete time-series, where Δ_t is an arbitrary instant, and t an index of a set member. Let further consider a set $\{\mathbf{L}\}$ that contains of all possible member pairs between $\{\mathbf{P}_{\Delta_t}\}$ and $\{\mathbf{Q}_{\Delta_t}\}$ such that $\{\mathbf{L}\}$=$\{(P_{a_1}, Q_{b_1}), \ldots, (P_{a_m}, Q_{b_m})\}_{\{\{\Delta_1\leq a_i\leq\Delta_p\};\, \{\Delta_1\leq b_i\leq\Delta_q\};\, \{1\leq i\leq m\text{-}1\}\}}$. Then, the *discrete Fréchet distance*, δ_{dF}, whose value depends on the values (position) and order of the set members, is defined as follows:

$$\delta_{dF}(\mathbf{P}_{\Delta_t}, \mathbf{Q}_{\Delta_t}) = \min_{\mathbf{L}} \left(\max_{i=1,\ldots,m} |P_{a_i} - Q_{b_i}| \right) \tag{A.51}$$

For identical sets δ_{dF}=0 whilst a rise in δ_{dF} indicates an increase in dissimilarities. In addition, it should be noted that the discrete Fréchet distance is an approximation to the Fréchet distance to allow easier code implementation and lower computational costs.

Appendix A.5. Fourier transformation of some filter kernels

Appendix A.5.1. Gaussian-form autocorrelation function

The Fourier transform of a Gaussian function can be derived as follows [73]:

$$\mathscr{F}_x\left\{\exp\left[-\frac{\pi}{c}\frac{x^2}{\mathrm{L}^2}\right]\right\}(\kappa) = \mathscr{F}_x\left\{\exp\left[-ax^2\right]\right\}(\kappa) \qquad a \leftrightarrow \pi c^{-1}\mathrm{L}^{-2} \tag{A.52a}$$

$$= \int_{-\infty}^{\infty} \exp\left[-ax^2\right]\, \exp\left[-2\pi i\kappa x\right] dx \tag{A.52b}$$

$$= \int_{-\infty}^{\infty} \exp\left[-ax^2\right]\, \left[\cos(2\pi\kappa x) - i\sin(2\pi\kappa x)\right] dx \tag{A.52c}$$

$$= \int_{-\infty}^{\infty} \exp\left[-ax^2\right]\, \cos(2\pi\kappa x)\, dx \; - i \int_{-\infty}^{\infty} \exp\left[-ax^2\right]\, \sin(2\pi\kappa x)\, dx \tag{A.52d}$$

$$= \sqrt{\pi\, a^{-1}} \exp\left[-\frac{\pi^2\kappa^2}{a}\right] \tag{A.52e}$$

$$= \sqrt{c}\,\mathrm{L}\, \exp\left[-c\pi\mathrm{L}^2\kappa^2\right] \qquad a \leftrightarrow \pi c^{-1}\mathrm{L}^{-2} \tag{A.52f}$$

where $\mathscr{F}_x$ is the Fourier transform operator on the variable x, $\mathrm{L}\,[m(2\pi)^{-1}]$ the integral length-scale, $\kappa\,[(2\pi)m^{-1}]$ the spatial wavenumber, and c a model constant, for instance in Eq. 4 c=4. The first term of Eq. A.52d reduces to Eq. A.52e [73], and its second term goes to zero due to the symmetrical integration of the odd function [73].

Appendix A.5.2. Exponential-form autocorrelation function

The Fourier transform of an exponential function is derived as follows [74]:

$$\mathscr{F}_x\left\{\exp\left[-\frac{\pi}{c}\frac{x}{\mathrm{L}}\right]\right\}(\kappa) = \mathscr{F}_x\left\{\exp\left[-ax\right]\right\}(\kappa) \qquad a \leftrightarrow \pi c^{-1}\mathrm{L} \tag{A.53a}$$

$$= \int_{-\infty}^{\infty} \exp\left[-ax\right]\,\exp\left[-2\pi i\kappa x\right]dx \tag{A.53b}$$

$$= \int_{-\infty}^{0} \exp\left[-2\pi i\kappa x\right]\,\exp\left[2\pi ax\right]dx + \int_{0}^{\infty} \exp\left[-2\pi i\kappa x\right]\,\exp\left[-2\pi ax\right]dx \tag{A.53c}$$

$$= \int_{-\infty}^{0} \left[\cos(2\pi\kappa x)-i\sin(2\pi\kappa x)\right]\,\exp\left[2\pi ax\right]dx + \int_{0}^{\infty} \left[\cos(2\pi\kappa x)-i\sin(2\pi\kappa x)\right]\,\exp\left[-2\pi ax\right]dx \tag{A.53d}$$

$$(-x \leftrightarrow u; -dx \leftrightarrow du) \qquad = \int_{0}^{\infty} \left[\cos(2\pi\kappa u)+i\sin(2\pi\kappa u)\right]\,\exp\left[-2\pi au\right]du + \int_{0}^{\infty} \left[\cos(2\pi\kappa u)-i\sin(2\pi\kappa u)\right]\,\exp\left[-2\pi au\right]du \tag{A.53e}$$

$$= 2\int_{0}^{\infty} \cos(2\pi\kappa u)\,\exp\left[-2\pi au\right]du \quad \rightarrow \int_{0}^{\infty} \cos(\kappa u)\,\exp\left[-bu\right]du = \frac{b}{b^2+\kappa^2} \tag{A.53f}$$

$$= \quad \cdots \tag{A.53g}$$

$$= \frac{2c\mathrm{L}\pi^{-1}}{(2c\mathrm{L}\kappa)^2+1} \qquad a \leftrightarrow \pi c^{-1}\mathrm{L} \tag{A.53h}$$

where $\mathscr{F}_x$ is the Fourier transform operator on the variable $\{x\}_{\{x>0\}}$, $\mathrm{L}\left[m(2\pi)^{-1}\right]$ the integral length-scale, $\kappa\left[(2\pi)m^{-1}\right]$ the spatial wavenumber, and c a model constant, for instance in Eq. 7 c=2.

Appendix A.6. Size of extra random numbers due to the spatial variation of scales

Consider a planar synthetic turbulence generation grid that has n nodes. Let the grid is divided into x zones which are assumed having the same number of nodes, n/x. Also assume that a scale set, which contains k number of scales, is input for each zone. The following relations then can be presented among the size of random number set required for "*valid*" type of convolution summations

on an undivided grid, M_1, and on a zone, M_2, and the filter support of the scale N_1:

$$\begin{aligned} n &= \mathrm{M}_1 - \mathrm{N}_1 + 1 \\ \mathrm{M}_2 - \mathrm{N}_1 + 1 &= \frac{\mathrm{M}_1 - \mathrm{N}_1 + 1}{x} \qquad \text{for a zone} \\ x\mathrm{M}_2 - x\mathrm{N}_1 + x &= \mathrm{M}_1 - \mathrm{N}_1 + 1 \\ x\mathrm{M}_2 - \mathrm{M}_1 &= (x-1)(\mathrm{N}_1 - 1) \end{aligned} \tag{A.54}$$

where $x\mathrm{M}_2 - \mathrm{M}_1$ is the size of new random sets that needs to be generated for the whole grid for a single scale per time-step.